



1 **Antiphase dynamics between cold-based glaciers in the Antarctic**

2 **Dry Valleys region and ice extent in the Ross Sea during MIS 5**

3 Jacob T.H. Anderson¹, Toshiyuki Fujioka², David Fink³, Alan J. Hidy⁴, Gary S.

4 Wilson^{1,5}, Klaus Wilcken³, Andrey Abramov⁶, Nikita Demidov⁷

5 ¹Department of Marine Science, University of Otago, PO Box 56, Dunedin, New Zealand

6 ²Centro Nacional de Investigación sobre la Evolución Humana, Burgos 09002, Spain

7 ³Australian Nuclear Science & Technology Organisation, New Illawarra Road, Lucas Heights,

8 NSW, 2234, Australia

9 ⁴Center for Accelerator Mass Spectrometry, Lawrence Livermore National Laboratory,

10 Livermore CA 94550, USA

11 ⁵GNS Science, PO Box 30368, Lower Hutt 5040, Wellington, New Zealand

12 ⁶Institute of Physicochemical and Biological Problems of Soil Science, Pushchino, Russia

13 ⁷Arctic and Antarctic Research Institute, St. Petersburg, Russia

14 *Correspondence to:* Jacob T.H. Anderson (jacob.anderson@otago.ac.nz)

15 **Abstract**

16 During the interglacial and interstadials of Marine Isotope Stage 5 (MIS 5e, 5c, 5a), outlet
17 and alpine glaciers in the Dry Valleys region, Antarctica, appear to have advanced in
18 response to increased precipitation from enhanced open ocean conditions in the Ross Sea.
19 We provide further evidence of this antiphase behaviour through retreat of a peripheral lobe
20 of Taylor Glacier in Pearse Valley, a region that was glaciated during MIS 5. We measured
21 cosmogenic ¹⁰Be and ²⁶Al in three granite cobbles from thin, patchy drift (Taylor 2 Drift)
22 in Pearse Valley to constrain the timing of retreat of Taylor Glacier. Assuming simple
23 continuous exposure, our minimum, zero erosion, exposure ages suggest Taylor Glacier
24 partially retreated from Pearse Valley no later than 65–74 ka. Timing of retreat after 65 ka
25 and until the Last Glacial Maximum (LGM) when Taylor Glacier was at a minimum position,
26 remains unresolved. The depositional history of permafrost sediments buried below Taylor 2
27 Drift in Pearse Valley was obtained from ¹⁰Be and ²⁶Al depth profiles to ~3 metres in
28 permafrost in proximity to the cobble sampling sites. Depth profile modelling gives a
29 depositional age for near-surface (<1.65 m) permafrost at Pearse Valley of 180 ka⁺²⁰ / -40 ka,
30 implying deposition of permafrost sediments predate MIS 5 advances of Taylor Glacier.
31 Depth profile modelling of deeper permafrost sediments (>2.09 m) indicates a depositional



32 age of >180 ka. The cobble and permafrost ages reveal Taylor Glacier advances during MIS
33 5 were non-erosive or mildly erosive, preserving the underlying permafrost sediments and
34 peppering boulders and cobbles upon an older, relict surface. Our results are consistent with
35 U/Th ages from central Taylor Valley, and suggest changes in moisture delivery over Taylor
36 Dome during MIS 5e, 5c and 5a appear to be associated with the extent of the Ross Ice
37 Shelf and sea ice in the Ross Sea. At a coastal, lower elevation site in neighbouring Lower
38 Wright Valley, ^{10}Be and ^{26}Al depth profiles from a second permafrost core exhibit near-
39 constant concentrations with depth, and indicate the sediments are either vertically mixed
40 after deposition, or are sufficiently young and post-depositional nuclide production is
41 negligible relative to inheritance. $^{26}\text{Al}/^{10}\text{Be}$ concentration ratios for both depth profiles range
42 between 4.0 and 5.2 and are all lower than the nominal surface production rate ratio of 6.75
43 indicating that prior to deposition, these sediments experienced a complex exposure-burial
44 history. Assuming a single cycle exposure-burial scenario, the observed $^{26}\text{Al}/^{10}\text{Be}$ ratios are
45 equivalent to a total minimum exposure-burial history of ~1.2 Ma. Our new data corroborates
46 antiphase behaviour between outlet and alpine glaciers in the Dry Valleys region and ice
47 extent in the Ross Sea. We suggest a causal relationship of cold-based glacier advance and
48 retreat that is controlled by an increase in moisture availability during retreat of sea ice and
49 perhaps the Ross Ice Shelf, and conversely, a decrease during times of sea ice and Ross
50 Ice Shelf expansion in the Ross Sea.

51

52 **1 Introduction**

53 During Plio-Pleistocene warm intervals, the West Antarctic Ice Sheet (WAIS), and marine-
54 based sectors of the East Antarctic Ice Sheet (EAIS) underwent extensive retreat (Naish et
55 al., 2009; Pollard & DeConto, 2009; Cook et al., 2013; Blackburn et al., 2020; Patterson et
56 al., 2014). Warmer than present global temperatures and higher than present sea levels are
57 also observed in recent prominent interglacial periods, i.e., MIS 31 (~1.07 Ma), MIS 11 (~400
58 ka), and MIS 5e (130 - 115 ka) (Dutton et al., 2015; Naish et al., 2009; Pollard & DeConto,
59 2009). The extent of ice sheet retreat during these recent warm intervals varied significantly
60 within different drainage basins and through time. During the penultimate interglacial (MIS
61 5e), the average global temperature was ~1–2°C warmer than pre-industrial (Fischer et al.,
62 2018; Otto-Bliesner et al., 2013), Antarctic temperatures were ~3–5°C warmer (Jouzel et al.,
63 2007) and global mean sea levels were ~6–9 metres higher than present (Dutton &
64 Lambeck, 2012; Kopp et al., 2009). With a global average temperature currently ~1.1°C
65 warmer than pre-industrial levels, and predicted to be $\geq 1.5^\circ\text{C}$ in the coming decades (IPCC,
66 2021), interglacial conditions, such as during MIS 5, are an important analogue for



67 evaluating future ice sheet behaviour and global climate processes under future warming
68 scenarios.
69

70 Ice sheet modelling during the Last Interglacial (MIS 5e, 130–115 ka), projected Antarctic ice
71 loss contributed ~3.5–7.5 m GMSL (global mean sea level), primarily from WAIS retreat
72 (DeConto & Pollard, 2016; DeConto et al., 2021; Golledge et al., 2021; Turney et al., 2020).
73 Simulated ice sheet retreat by Golledge et al. (2021) suggested ice loss in the Thwaites and
74 Pine Island sector of the WAIS, whereas the Ross Ice Shelf remained intact. In contrast,
75 simulations by DeConto et al. (2016), and Turney et al. (2020) suggested retreat of the Ross
76 Ice Shelf, followed by retreat of the WAIS interior.
77

78 The $\delta^{18}\text{O}$ ice core records from Talos Dome reveal the EAIS was relatively intact during MIS
79 5 (Sutter et al., 2020) and recent studies suggest partial ice sheet lowering in Wilkes
80 Subglacial Basin but no grounding line retreat (Fig. 1; Golledge et al., 2021; Sutter et al.,
81 2020; Wilson et al., 2018). Ice core studies reveal increased accumulation rates at Taylor
82 Dome (Steig et al., 2000) and the Allan Hills Blue Ice Area (Yan et al., 2021) near the onset
83 of the Last Interglacial. Yan et al. (2021) hypothesized that high accumulation rates during
84 warm interglacials may reflect open ocean conditions in the Ross Sea, caused by reduced
85 sea ice extent, and possibly retreat of the Ross Ice Shelf relative to its present-day position.
86 This hypothesis is supported by a depleted $\delta^{18}\text{O}$ value (-0.175‰) from ice core records at
87 Roosevelt Island, indicating high sea level and reduced ice sheets during MIS 5a (Lee et al.,
88 2020).

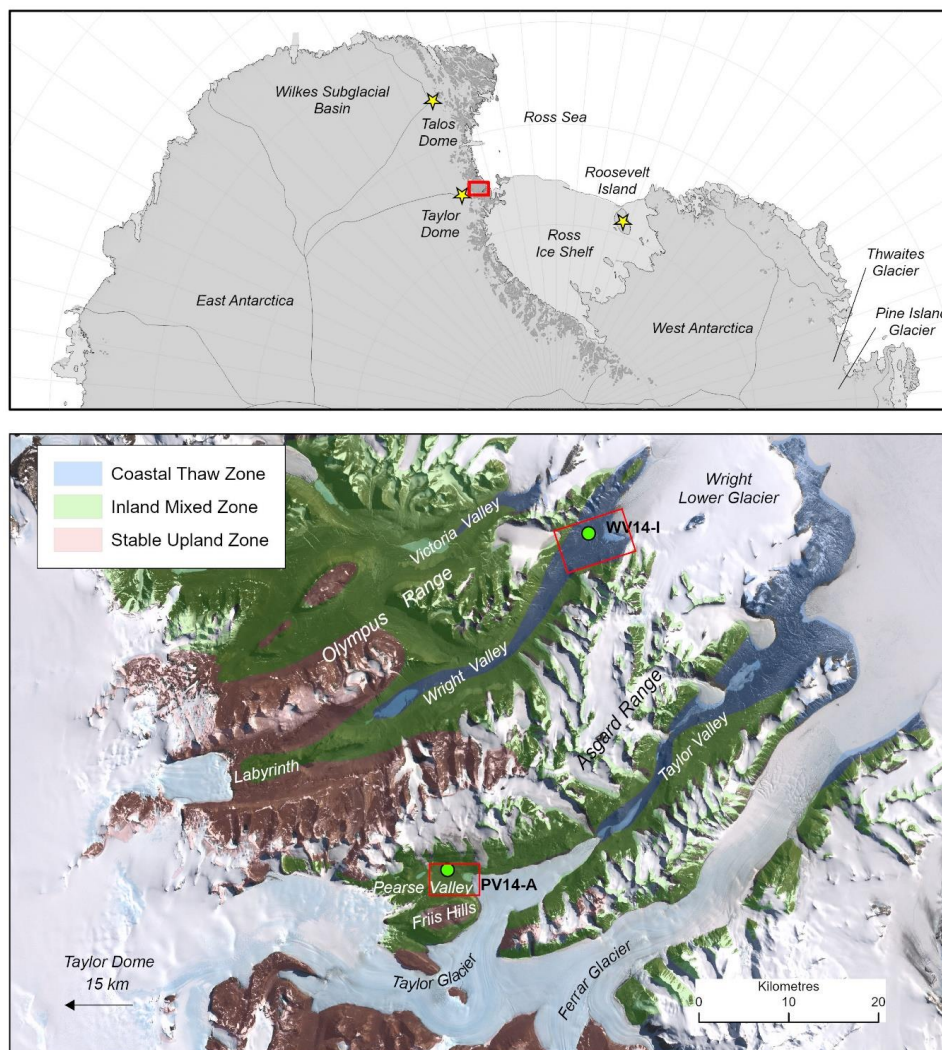
89 Terrestrial evidence from the Dry Valleys suggests Taylor and Ferrar glaciers were larger
90 than present during globally warm mid-Pliocene climatic optimum (3.0–3.1 Ma), MIS 31 (1.07
91 Ma) (Swanger et al., 2011) and MIS 5 (Brook et al., 1993; Higgins et al., 2000a). The glacier
92 advances appear to be out of phase with WAIS retreat and ocean warming during
93 interglacial periods. Alpine glaciers in the Dry Valleys also appear out of phase with marine
94 based ice sheet retreat and advanced during MIS11 (Swanger et al., 2017), MIS 5 (Swanger
95 et al., 2019), and MIS 3 (Joy et al., 2017). Glacial deposits and moraines, which can be used
96 to reconstruct past ice extent, have been preserved where cold-based glaciers have
97 advanced and retreated during Quaternary glaciations. The past ice volume and extent of
98 Taylor Glacier (during interglacial periods) has been derived from cosmogenic nuclide
99 studies and mapping drift and moraine deposits in lower Kennar Valley (Swanger et al.,
100 2011), and lower Arena Valley (Brook et al., 1993; Marchant et al., 1994), and U/Th dating in
101 central Taylor Valley (Higgins et al., 2000a). MIS 5 age glacial deposits in central Taylor
102 Valley and Arena Valley are mapped as Taylor 2 Drift (Bockheim et al., 2008; Brook et al.,



103 1993; Cox et al., 2012; Denton et al., 1970), termed Bonney Drift by Higgins et al. (2000b).
104 By inference, glacial deposits on the valley floor of Pearse Valley are mapped as Taylor 2
105 Drift (Bockheim et al., 2008; Cox et al., 2012; Denton et al., 1970). U/Th ages of algal
106 carbonates in central Taylor Valley suggest multiple advance / retreat cycles of the Taylor
107 Glacier snout during MIS 5, with retreat of Taylor Glacier continuing after the MIS 5/4
108 transition (Higgins et al., 2000a). The $\delta^{18}\text{O}$ values measured from buried ice in northern
109 Pearse Valley also support the advance of Taylor Glacier during MIS 5 (Swanger et al.,
110 2019). However, the timing of advance and retreat of Taylor Glacier in central Taylor Valley
111 and in Pearse Valley remain poorly constrained.

112 Previous studies investigating chronology and stability of glacial drift deposits, sediments
113 and permafrost in the Dry Valleys and Transantarctic Mountains typically focused on high
114 elevation sites (e.g., Bergelin et al., 2022; Bibby et al., 2016; Morgan et al., 2011; 2010; Ng
115 et al., 2005; Schäfer et al., 2000; Sugden et al., 1995). The objective of these studies has
116 largely been to constrain the ages and / or erosion and sublimation rates of early
117 Pleistocene, Pliocene, and Miocene landscapes. There only appears to be one study
118 investigating the age and stability of permafrost below 1000 m elevation (Morgan et al.,
119 2010). Yet, understanding the depositional environment and stability of permafrost at low
120 elevations is important for interpreting landscape evolution, geomorphic processes and polar
121 climate change on Earth, and as a terrestrial analogue for Mars (e.g., Marchant & Head,
122 2007).

123 Here, we investigate the relationship between thin, patchy drift overlying permafrost
124 sediments in Pearse Valley. Thin, patchy drift is the only evidence of cold-based glacier
125 overriding, and is defined as a scattering of clasts overlying older, undisturbed desert
126 pavements (Atkins, 2013). We present cosmogenic nuclide surface exposure ages from
127 three cobbles in Pearse Valley to determine the age of Taylor 2 Drift, and provide constraints
128 on the timing of retreat of a peripheral lobe of Taylor Glacier during MIS 5. To determine
129 the relationship between the thin, patchy drift and underlying permafrost sediments at
130 Pearse Valley, we also present companion ^{10}Be and ^{26}Al depth profiles of permafrost.
131 Combining exposure ages of cobbles from the drift and permafrost depth profiles, we
132 constrain a minimum age of Taylor Glacier retreat, and infer the depositional history of the
133 permafrost sediments. These data from Pearse Valley provide insight into Taylor Glacier
134 behaviour and associated geomorphic processes during MIS 5. Additionally, we present ^{10}Be
135 and ^{26}Al permafrost depth profiles from a coastal, lower elevation site in the neighbouring
136 Lower Wright Valley, and together with the Pearse Valley depth profiles, discuss long-term
137 recycling processes of Dry Valleys sediments.



138

139 **Figure 1.** Study area and location of Dry Valleys. Yellow stars show ice core sites discussed
140 in the text. The green circles show the locations of the Pearse Valley and Lower Wright
141 Valley sites where permafrost cores were recovered. The three microclimatic zones are the
142 stable upland zone (brown), inland mixed zone (green), and coastal thaw zone (blue).
143 Modified from Marchant and Head (2007); and Salvatone and Levy (2021). Red rectangles
144 in the lower diagram show the locations of Pearse Valley in Fig. 2 and Lower Wright Valley
145 in Fig. 3.

146

147 2 Geologic setting and study area



148 The Dry Valleys are a hyperarid, cold polar desert and can be subdivided into three
149 geographic zones (stable upland, inland mixed, and coastal thaw zones), which are defined
150 by their microclimatic parameters of atmospheric temperature, soil moisture, and relative
151 humidity (Fig. 1; Marchant & Denton, 1996; Marchant & Head, 2007). The stability and
152 evolution of geomorphic features and permafrost are controlled by subtle variations within
153 each microclimatic zone. The active-layer in permafrost is defined as soil horizons where the
154 ground temperature fluctuates above and below 0°C seasonally (Davis, 2001; Yershov,
155 1998). Antarctic permafrost soils along the floors and flanks of ice-free valleys are vertically
156 mixed, initially through deposition of reworked sediments, and secondarily through active-
157 layer cryoturbation up to 70 cm depth of the surface (Bockheim et al., 2007; 2008).
158 Cryoturbation is defined as soil movement due to repeated freeze–thaw, generally within the
159 active-layer of permafrost (French, 2017). Active-layers can be distinguished by the
160 presence (wet active-layer) or absence (dry active-layer) of water. Soils in the coastal thaw
161 zone are seasonally moist and comprise wet active-layers, whereas soils in the inland mixed
162 zone are dry and comprise dry active-layers (Marchant & Head, 2007). Our study sites
163 focused on two different microclimatic zones (Fig. 1); Pearse Valley in the inland mixed
164 zone, and Lower Wright Valley in the coastal thaw zone, which differ in age, elevation, and
165 distance from the coast.

166 **2.1 Pearse Valley**

167 Pearse Valley is an ice-free valley that is bounded by the Friis Hills in the south, the Asgard
168 Range in the north and opens onto peripheral lobes of Taylor Glacier in the east and west
169 (Fig. 1). Taylor Glacier flows east from Taylor Dome of the EAIS, terminating in Taylor
170 Valley. At the eastern end of Pearse Valley, a lobe of Taylor Glacier terminates into Lake
171 Joyce, a closed-basin proglacial lake (Fig. 2). Taylor Glacier and local alpine glaciers have
172 advanced in the present interglacial and occupy their maximum position since the Last
173 Glacial Maximum (LGM) (Higgins et al., 2000a). At the head of Pearse Valley, glacially
174 incised bedrock sits at a similar elevation to the Labyrinth platform in upper Wright Valley,
175 likely formed by a network of subglacial drainage channels beneath wet-based glacial
176 conditions during the Miocene Climate Transition (Fig. 1; Lewis & Ashworth, 2016; Chorley
177 et al., 2022). The northern valley wall comprises gelifluction lobes, buried snowpack
178 deposits, meltwater channels derived from ephemeral streams, and fans fed by the
179 meltwater channels in front of the lobes (Heldmann et al., 2012; Swanger et al., 2019). The
180 valley floor consists of a lower elevation area on the southern side, and a higher elevation
181 area on the northern side of the valley. The PV14-A core and cobble samples are located on
182 the central northern side of the valley floor (Fig. 2).

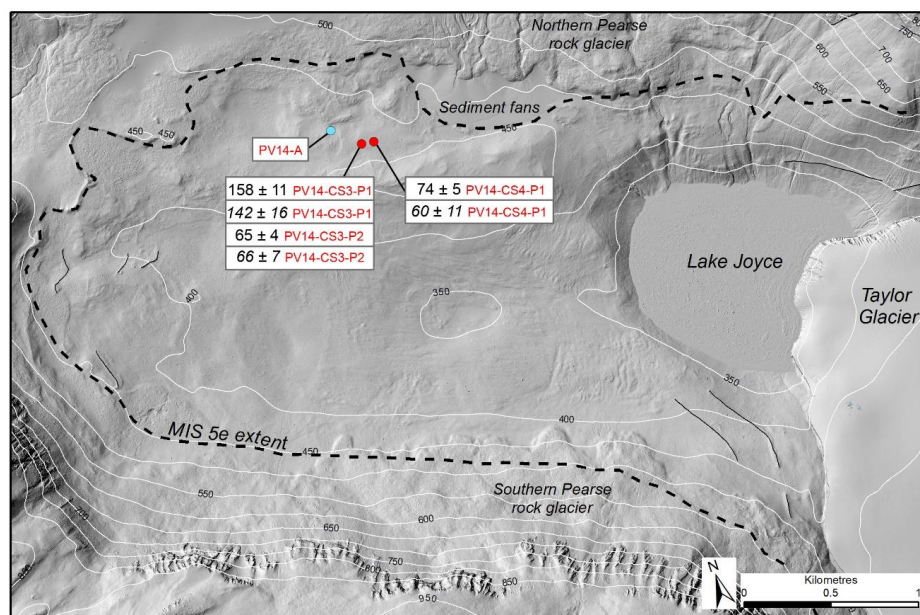


183 The local bedrock comprises basement granites and Ferrar dolerite intrusives (Cox et al., 2012;
184 Gunn & Warren, 1962). Glacial deposits on the valley floor are mapped as Taylor 2 Drift
185 (Bockheim et al., 2008; Denton et al., 1970). These sediments were inferred as waterlain and
186 melt-out tills following the penultimate down-valley advance of the Taylor Glacier during MIS 5
187 (70 – 130 ka) (Cox et al., 2012; Higgins et al., 2000a; Swanger et al., 2019). The valley floor
188 landscape is characterized by hummocky moraines with a combination of glacial, and fluvial
189 deposits, and aeolian sediments. Variably weathered granite boulders (up to 3 m in diameter)
190 form a lag deposit on the drift surface, inferred as a till deflation or a separate younger
191 depositional unit (Higgins et al., 2000b). The northern and southern Pearse Valley walls
192 comprises extensive rock glaciers (Swanger et al., 2019).

193

194 **2.1.1 Modern climate**

195 Pearse Valley is situated in the inland mixed zone of the Dry Valleys (Marchant & Denton,
196 1996). The valley has a mean annual temperature of -18°C (Marchant et al., 2013) and
197 precipitation rates of 20–50 mm/yr (water equivalent), and 100–200 mm/yr in the adjacent
198 Asgard Range, the source region for the local alpine glaciers (Fountain et al., 2010). Mean
199 summer air temperatures (December through February) in Pearse Valley are -2 to -7°C
200 (Marchant et al., 2013). Ground surface temperatures measured at the Pearse Valley
201 meteorological station between 27–28 November, 2009, recorded a peak temperature of 10°C
202 due to solar heating (Heldmann et al., 2012). Winds in Pearse Valley are strong enough to
203 mobilise sand grains and form aeolian surface features such as sand dunes (Heldmann et al.,
204 2012).



205

206 **Figure 2.** Map of Pearse Valley with MIS 5e extent of Taylor Glacier (black dashed line; Cox
207 et al. 2012), sample locations and PV14-A permafrost drill site. Thin black lines trace
208 undated moraines. PV14-A drill site (blue circle) and measured ^{10}Be and ^{26}Al (italics) ages of
209 cobbles residing on boulders are shown in kiloyears with 1σ uncertainties (red circles). Lidar
210 image from Fountain et al. (2017).

211

212 2.2 Lower Wright Valley

213 Lower Wright Valley is ice-free and is bounded by the Asgard Range in the south, and the
214 Olympus Range in the north (Fig. 1). The mouth of the valley at the eastern end is cut off from
215 the Ross Sea by the Wright Lower Glacier, a lobe of the Wilson Piedmont Glacier. Lake
216 Brownworth, a proglacial lake fed by the Wright Lower Glacier, supplies the westward flowing
217 Onyx River. The WV14-I core is located on the northern side of Lower Wright Valley (Fig. 3).
218 Radiocarbon dates of lacustrine algae from glaciolacustrine deposits suggest Lake
219 Brownworth is a small remnant of a much larger lake that existed during the LGM and early
220 Holocene (Hall et al., 2001). The post-glacial, Holocene age landscapes form hummocky
221 moraines, with a combination of deltas, shorelines and glaciolacustrine sediments (Hall et al.,
222 2001). Glacial meltwater streams drain into Lake Brownworth and the Onyx River from the
223 north and south valley walls. The local bedrock comprises basement metasediments and
224 granites, and Ferrar dolerite intrusives (Cox et al., 2012). Metasediments, granite, dolerite and
225 occasional basalt sediments in the Lower Wright Valley have accumulated since the last

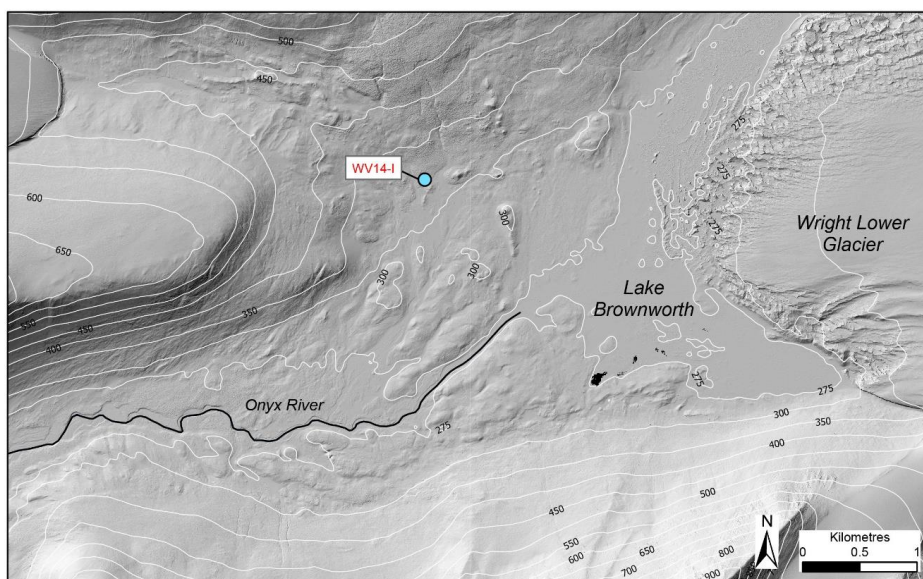


226 deglaciation by lacustrine, fluvial and aeolian processes (Hall et al., 2001; Hall & Denton,
227 2005).

228

229 2.2.1 Modern climate

230 Lower Wright Valley is situated in the coastal thaw zone of the Dry Valleys (Marchant &
231 Denton, 1996) and has a mean annual temperature of -21°C (Doran et al., 2002) and
232 precipitation rates of 26–51 mm/yr (water equivalent) (Fountain et al., 2010). Mean summer
233 air temperatures (December through February) in Lower Wright Valley are -5 to -7°C , and can
234 exceed 0°C for >6 days per year (Doran et al., 2002). Meltwater forms during summer months
235 (December and January) when temperatures can rise to as much as 10°C at some locations
236 (Hall et al., 2001).



237

238 **Figure 3.** Map of Lower Wright Valley and WV14-I permafrost drill site (blue circle). Lidar
239 image from Fountain et al. (2017).

240

241 3 Methods

242 3.1 Surface exposure sample collection

243 Three granite cobble samples were collected for surface exposure analysis from Pearse
244 Valley (Table 1; Fig. 2). We targeted perched cobbles, resting on larger flat boulders to



245 minimise the possibility of post-depositional disturbance and hence best reflect deposition
246 from retreating glacier ice or from surface deflation through sublimation. Samples that
247 showed minimal weathering or fracturing were selected. The three cobbles were perched on
248 larger host boulders (>1 m diameter) which were elevated above the local surface
249 permafrost valley deposits (Fig. 4). Two samples (PV14-CS3-P1 and PV14-CS3-P2) are
250 small cobbles perched on the same host boulder, while the third sample (PV14-CS4-P1) is a
251 slightly larger cobble perched on a different host boulder less than 80 metres away.



252

253 **Figure 4.** Boulders and cobbles from Taylor 2 Drift on the central northern side of Pearse
254 Valley. (a) PV14-CS3-P1 and PV14-CS3-P2 cobbles perched on a dolerite boulder. (b)
255 Close view of PV14-CS3-P2. (c) PV14-CS4-P1 cobble hosted on dolerite boulder. (d) A
256 granite boulder, hosting a dolerite boulder.

257

258 3.2 Permafrost core locations and characteristics

259 During the 2014/15 austral field season, permafrost cores were recovered from Pearse
260 Valley and Lower Wright Valley using a gasoline powered dry drilling technique (Fig. 1).
261 These two cores were sampled for sedimentological and for cosmogenic nuclide analysis.
262 After extraction, the core sections were divided into ~10 cm portions for sub-sampling and



263 analysis. Permafrost sediments were collected in a combination of Whirl-Pak bags and PVC
264 core liners.

265

266 **3.2.1 Pearse Valley borehole core**

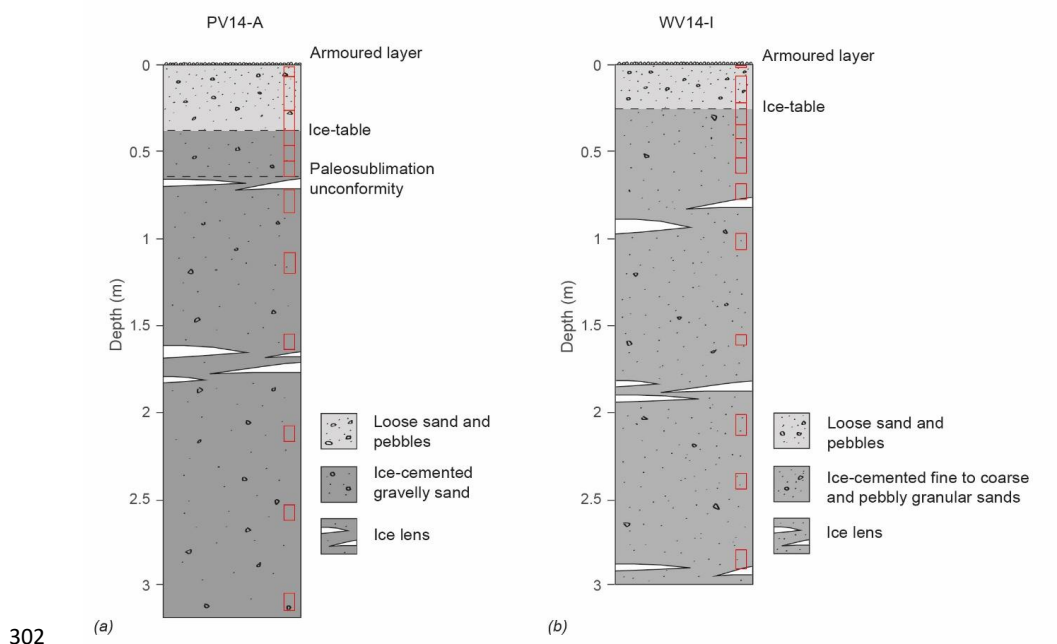
267 The PV14-A core is located on an elevated bench that extends along the northern side of
268 the valley floor at 450 masl (77.7062°S, 161.5467°E), ~3 km north-west of the present
269 position of the Taylor Glacier lobe (Fig. 2). The core was recovered to a depth of 3.16 m (Fig
270 5a; Table 2). The active-layer above the ice-cemented permafrost consists of a thin
271 armoured surface layer of desert pavement (~0.02 m thick), which caps a layer of loose dry
272 sand (~0.35 m thick). Recovered sediments from beneath the armoured desert pavement
273 comprise a dry active-layer of loose sand and pebbles down to 0.37 m depth. Below 0.37 m
274 depth the recovered sediments comprise ice-cemented permafrost. The ¹⁰Be and ²⁶Al depth
275 profiles start below the 0.02 m thick surface armoured pavement. The first three samples
276 were collected from the dry active-layer and nine from the ice-cemented permafrost (Fig.
277 5a). Sediments within the permafrost core comprise gravelly sands derived from weathered
278 Beacon Supergroup, granite, granodiorite, diorite, and dolerite origins, which are
279 structureless, or weakly bedded. Between 0.73–0.86 m depth, the core comprises several
280 ice lenses indicative of ice accumulation below a paleosublimation unconformity. Several
281 small ice lenses were also recovered between 1.57–1.87 m depth. Only two of the three
282 active-layer samples, and six of the nine permafrost core samples were successful in
283 providing paired ¹⁰Be and ²⁶Al concentrations.

284 **3.2.2 Lower Wright Valley borehole core**

285 The WV14-I core is located in eastern Wright Valley at 326 masl (77.4252°S, 162.6664°E),
286 ~2 km west of Wright Lower Glacier (Fig. 3). The core was recovered to a depth of 2.91 m
287 (Fig. 5b; Table 2). The active-layer above the ice-cemented permafrost consists of a thin
288 armoured surface layer of desert pavement (~0.02 m thick), which caps a layer of loose
289 sand and pebbles (~0.26 m thick). Below 0.28 m depth the recovered sediments comprised
290 ice-cemented permafrost. The ¹⁰Be and ²⁶Al depth profiles start on the armoured desert
291 pavement. Two samples were collected from the active-layer and 10 from the ice-cemented
292 permafrost (Fig. 5b). The permafrost sediments are structureless, to thinly laminated, fine to
293 coarse, and pebbly granular sands, which we interpret to be fluvial and aeolian deposits.
294 Sediments within the core are derived from weathered granite, metasedimentary, dolerite
295 and basalt origins. From 0–0.98 m depth, core sections were broken and loose sediment
296 was recovered. Sediments recovered from 0.98–2.91 m were ice-cemented, except when
297 encountering ice lenses. Several small ice lenses were recovered between 1.80–2.03 m



298 depth. Hall et al. (2001) suggested sediments at Lower Wright Valley are delta, shoreline
299 and glaciolacustrine deposits associated with a large proglacial lake at the LGM and in the
300 early Holocene (25–7 ka). Only four of the 10 permafrost core samples were successful in
301 providing paired ^{10}Be and ^{26}Al concentrations.



303 **Figure 5.** (a) Pearse Valley (PV14-A) permafrost core, and (b) Lower Wright Valley (WV14-I)
304 permafrost core sedimentology. Locations of cosmogenic nuclide samples shown in red
305 boxes.

306

307 3.3 Analytical methods

308 Each core sample processed for cosmogenic nuclide analysis was heated at 100°C
309 overnight to remove ice and dry the sediment. Dried core samples, and cobble surface
310 samples were crushed and sieved to obtain the 250 – 500 µm fraction. Quartz was
311 separated and purified using the hot phosphoric acid method (Mifsud et al., 2013) and
312 beryllium and aluminium were extracted from quartz via conventional HF dissolution and ion
313 exchange chromatography (Child et al., 2000). Isotope ratios were measured by Accelerator
314 Mass Spectrometry on the SIRIUS accelerator at the Australian Nuclear Science and
315 Technology Organisation (Wilcken et al., 2019).

316 Measured $^{10}\text{Be}/^9\text{Be}$ ratios were normalised to the 07KNSTD (KN-5.2) standard of Nishiizumi
317 et al. (2007) with a nominal $^{10}\text{Be}/^9\text{Be}$ ratio of 8560×10^{-15} . Measured $^{26}\text{Al}/^{27}\text{Al}$ ratios were



318 normalised to the KNSTD (KN-4.2) standard of Nishiizumi (2004) with a nominal $^{26}\text{Al}/^{27}\text{Al}$
319 ratio of 30960×10^{-15} . The nuclide concentration data for the perched cobbles, and Pearse
320 Valley and Lower Wright Valley depth profiles are shown in Tables 1 and 2, respectively. Full
321 procedural $^{10}\text{Be}/^9\text{Be}$ blanks were obtained using a solution processed from dissolved beryl
322 mineral with a known ^9Be concentration (1068 and 1048 $\mu\text{g/g}$ (solution)) and resulted in
323 ratios of $1.9 \pm 0.4 \times 10^{-15}$ and $1.3 \pm 0.3 \times 10^{-14}$. Blank corrections to measured $^{10}\text{Be}/^9\text{Be}$ ratios
324 amounted to <2%. Procedural $^{26}\text{Al}/^{27}\text{Al}$ blanks were processed from standard reference ICP
325 aluminium solutions (1000 $\mu\text{g/ml} \pm 1\%$) and resulted in ratios $3.6 \pm 1.7 \times 10^{-14}$ and 1.3 ± 0.6
326 $\times 10^{-15}$. Blank corrections to measured $^{26}\text{Al}/^{27}\text{Al}$ ratios amounted to 4 to 35% for Pearse Valley
327 erratics and <1% for all other samples. Final errors in ^{10}Be and ^{26}Al concentrations are
328 obtained by quadrature addition of the final AMS analytical error (the larger of the total
329 statistical or standard mean error), a reproducibility error based on the standard deviation of
330 the set of standard reference samples measured during the run (typically 1-2% for either
331 ^{10}Be or ^{26}Al), a 1% error in Be spike concentration and a representative 3% error for ICP Al
332 concentration of the native ^{27}Al in the final purified quartz powder. Unless otherwise stated,
333 all analytical uncertainties are 1σ .

334 Surface exposure ages for the cobble samples were calculated using version 3 of the
335 CRONUS-Earth calculator (<http://hess.ess.washington.edu/>; Balco et al., 2008) using the
336 LSDn scaling scheme (Lifton et al., 2014) and the primary default calibration data set of
337 Borchers et al. (2016) (Table 1). Complete analytical data for all measurements are shown in
338 Table S1, and data from surface samples are archived on the ICE-D Antarctica database
339 (<http://antarctica.ice-d.org>).

340

341 **3.4 Dual nuclide depth profile models and parameters**

342 ^{10}Be and ^{26}Al data from core samples were used to model the surface exposure age of
343 permafrost sediments at Pearse and Lower Wright valleys via the depth profile technique
344 (Anderson et al., 1996). We implemented a modified version of the Monte Carlo-based code
345 of Hidy et al. (2010) that allows profiles of both ^{10}Be and ^{26}Al to be modelled jointly (after Hidy
346 et al. (2018)). For shallow profiles in sediments, where non-unique solutions for exposure age
347 and erosion rate are likely, this approach allows estimation of exposure age and pre-
348 depositional nuclide concentration (i.e., inheritance) given reasonable observation-based
349 constraint on erosion rate or net erosion (e.g., Bergelin et al., 2022; Hidy et al., 2010, 2018;
350 Mercader et al., 2012; Morgan et al., 2010).

351 The simplest assumptions are that all depth profile sediments have the same inherited
352 nuclide concentration at the time of deposition and that post depositional sediment mixing is



353 absent. The former is a reasonable assumption for our core samples given that these
354 sediments comprise a combination of well mixed, thick glacial tills, fluvial and aeolian
355 sediments that were deposited at a given time when the ice retreated from each valley. As
356 described in Sect. 3.2 above, the upper ~0.3 m of both cores consists of loose sandy
357 sediment that is mobile or active. Fig. 6 shows the evolution of a cosmogenic nuclide depth
358 profile over time with the added feature of a near-constant ^{10}Be concentration in a
359 cryoturbated active-layer above ice-cemented permafrost sediments. Any post-depositional
360 nuclide production is unknown, but the inheritance determined by the best-fit depth profile
361 asymptote can be subtracted from the measured values for each sample (Hidy et al., 2018).

362 To ensure consistency with the cobble exposure ages, we obtain production rates applied in
363 the depth profile model from the CRONUS-Earth calculator. For the PV14-A core, we use a
364 site-specific spallation ^{10}Be surface production rate of $8.40 \text{ atoms } ^{10}\text{Be g}^{-1} (\text{quartz}) \text{ yr}^{-1}$, and a
365 ^{26}Al surface production rate of $59.7 \text{ atoms } ^{26}\text{Al g}^{-1} (\text{quartz}) \text{ yr}^{-1}$. For the WV14-I core, we use a
366 site-specific spallation ^{10}Be surface production rate of $7.47 \text{ atoms } ^{10}\text{Be g}^{-1} (\text{quartz}) \text{ yr}^{-1}$, and a
367 ^{26}Al surface production rate of $53.2 \text{ atoms } ^{26}\text{Al g}^{-1} (\text{quartz}) \text{ yr}^{-1}$. These production rates were
368 calculated using LSDn scaling (Lifton et al., 2014) and the primary calibration data set of
369 Borchers et al. (2016). These production rates yield $^{26}\text{Al}/^{10}\text{Be}$ surface production rate ratios of
370 7.11 and 7.12 for Pearse Valley and Lower Wright Valley, respectively. We assume a neutron
371 attenuation length of $140 \pm 5 \text{ g cm}^{-2}$, as used in previous Antarctic studies for ^{10}Be and ^{26}Al
372 (Bergelin et al., 2022; Borchers et al., 2016). Spallogenic production rate uncertainty has not
373 been included in the modelling. Muogenic production with depth, including an assumed 8%
374 uncertainty, followed Model 1A from Balco (2017). We assume bulk density to be constant
375 with depth but sampled from a normal distribution of $1.7 \pm 0.1 \text{ g cm}^{-3}$ based on bulk density
376 measured from two core samples. Erosion rate and net erosion were constrained between 0–
377 0.4 cm/ka and 400 cm, respectively, based on field observations described in Sect. 4.2.
378 Within these constraints, exposure age, surface erosion rate, and inheritance for ^{10}Be and
379 ^{26}Al were simulated with uniform distributions, and model output was based on $n=100,000$
380 acceptable depth profile solutions.

381
382
383
384
385
386
387
388



Table 1. Cosmogenic ^{10}Be and ^{26}Al concentrations and apparent exposure ages from Pearse Valley

Sample name	Latitude (DD)	Longitude (DD)	Elevation (masl)	Sample thickness (cm)	Topographic shielding	^{10}Be conc. (10^5 atoms g^{-1}) ^a	^{26}Al conc. (10^5 atoms g^{-1}) ^b	Apparent ^{10}Be exposure age (ka) ^{c,d}	Apparent ^{26}Al exposure age (ka) ^{c,d}	$^{26}\text{Al}/^{10}\text{Be}$ ratio	Erosion-corrected ^{10}Be exposure age (ka) ^e
PV14-CS3-P1	-77.70737	161.55283	451	6	0.993	12.40 ± 0.39	76.57 ± 4.48	158 ± 11 (5)	142 ± 16 (9)	6.18 ± 0.41	174 ± 13 (6)
PV14-CS3-P2	-77.70737	161.55283	451	3	0.993	5.36 ± 0.15	37.99 ± 1.54	65 ± 4 (2)	66 ± 7 (3)	7.09 ± 0.35	68 ± 5 (2)
PV14-CS4-P1	-77.70747	161.55582	451	5	0.993	5.94 ± 0.16	33.71 ± 5.14	74 ± 5 (2)	60 ± 11 (9)	5.68 ± 0.88	77 ± 5 (2)

All samples are granite cobbles and have a density of 2.65 g cm^{-3} .

^a Normalised to the 07KNSSTD (KN-5.2) standard of Nishiizumi et al. (2007).

^b Normalised to the KNSTD (KN-4.2) standard of Nishiizumi (2004).

^c Exposure ages calculated using the CRONUS-Earth calculator (<http://hess.ess.washington.edu/math/>), using the LSDn scaling scheme.

^d Both internal and external uncertainties (shown at the 1σ level). Internal uncertainties (given in parentheses) are analytical uncertainties only and external uncertainties are absolute uncertainties and include production rate and scaling errors.

^e Calculated using an erosion rate of 0.65 mm/ka .



391 **Table 2.** Depth profile data from Pearse Valley and Lower Wright Valley

Sample name	Sample depth (m)	¹⁰ Be conc. (10 ⁶ atoms g ⁻¹) ^a	²⁶ Al conc. (10 ⁶ atoms g ⁻¹) ^b	²⁶ Al/ ¹⁰ Be ratio
Pearse Valley				
PV14-SS-5	0.02 - 0.07	4.24 ± 0.095	-	-
PV14-A-01	0.07 - 0.27	4.37 ± 0.097	18.67 ± 0.73	4.27 ± 0.19
PV14-A-02	0.27 - 0.37	4.35 ± 0.097	17.97 ± 0.71	4.13 ± 0.19
PV14-A-03	0.37 - 0.47	4.42 ± 0.098	19.63 ± 0.82	4.44 ± 0.21
PV14-A-04	0.47 - 0.56	-	19.94 ± 0.78	-
PV14-A-05	0.56 - 0.65	4.40 ± 0.098	18.28 ± 0.69	4.16 ± 0.18
PV14-A-07	0.73 - 0.86	3.96 ± 0.089	17.95 ± 0.70	4.53 ± 0.20
PV14-A-10	1.09 - 1.21	-	16.38 ± 0.64	-
PV14-A-15	1.56 - 1.65	3.80 ± 0.085	15.09 ± 0.59	3.97 ± 0.18
PV14-A-20	2.09 - 2.18	3.98 ± 0.080	17.50 ± 0.66	4.40 ± 0.19
PV14-A-25	2.55 - 2.64	3.85 ± 0.086	16.70 ± 0.66	4.33 ± 0.20
PV14-A-30	3.06 - 3.16	-	16.76 ± 0.66	-
Lower Wright Valley				
WV14-SS-01	0 - 0.02	4.10 ± 0.092	22.89 ± 0.89	5.58 ± 0.25
WV14-I-01	0.07 - 0.23	3.73 ± 0.175	19.04 ± 0.75	5.10 ± 0.31
WV14-I-02	0.23 - 0.35	3.92 ± 0.088	18.43 ± 0.72	4.70 ± 0.21
WV14-I-03	0.35 - 0.43	4.00 ± 0.089	20.38 ± 0.77	5.09 ± 0.22
WV14-I-04	0.43 - 0.54	-	22.72 ± 0.89	-
WV14-I-05	0.54 - 0.63	-	21.66 ± 0.85	-
WV14-I-07	0.69 - 0.78	-	19.99 ± 0.79	-
WV14-I-10	0.98 - 1.07	4.09 ± 0.091	20.54 ± 0.81	5.02 ± 0.23
WV14-I-14	1.56 - 1.62	-	20.62 ± 0.81	-
WV14-I-20	2.02 - 2.14	4.22 ± 0.094	21.80 ± 0.86	5.17 ± 0.23
WV14-I-23	2.36 - 2.45	-	21.41 ± 0.84	-
WV14-I-29	2.80 - 2.91	-	13.60 ± 0.53	-

392

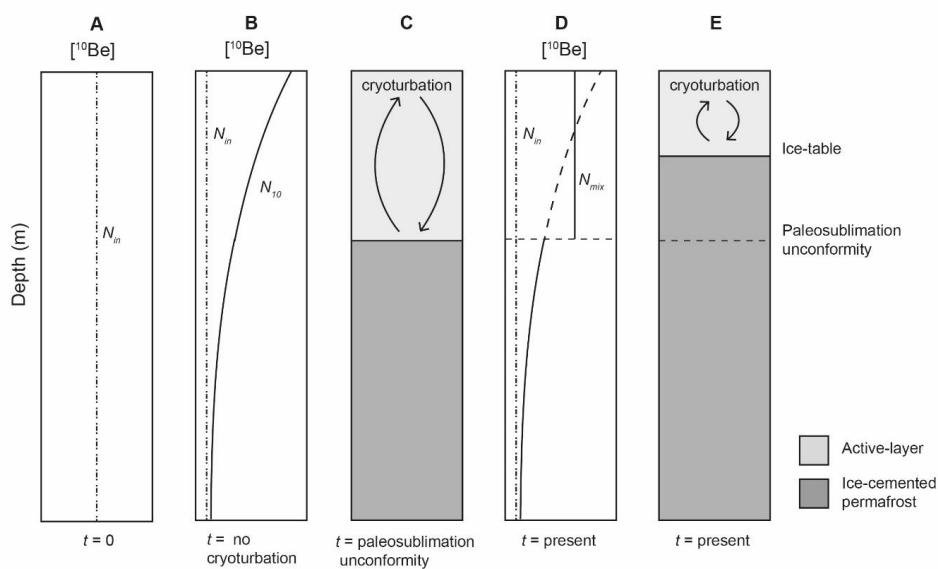
We assume a constant bulk density of 1.7 ± 0.1 g cm⁻³ based on bulk density measurements made on two core samples.

Topographic shielding is 0.9932 for Pearse Valley, and 0.9968 for Lower Wright Valley, respectively.

^a Normalised to the 07KNSTD (KN-5.2) standard of Nishiizumi et al. (2007).

^b Normalised to the KNSTD (KN-4.2) standard of Nishiizumi (2004).

393



394

395 **Figure 6.** Schematic representation of a ^{10}Be depth profile in permafrost modified by active-
396 layer cryoturbation. (a) Initial ^{10}Be profile (constant with depth) in well-mixed glacial till or
397 sediment. All quartz grains are assumed to have been deposited with a common nuclide
398 inheritance (N_m). (b) After prolonged exposure and in the absence of sediment mixing, an
399 exponentially decreasing nuclide depth profile is obtained. (c) Permafrost profile during an
400 interval where air temperature is warmer than present allowing near surface sediments to
401 form an active-layer above the paleo-sublimation depth. Sediments below the unconformity
402 are perennially frozen. (d) Vertical mixing via active-layer cryoturbation results in an average
403 ^{10}Be value (N_{mix}). A decreasing ^{10}Be profile remains below the unconformity. (e) Present-day
404 permafrost profile with shallower active-layer and ice-table than shown in (c).

405

406 4 Results

407 4.1 Surface exposure ages and erosion rates at Pearse Valley

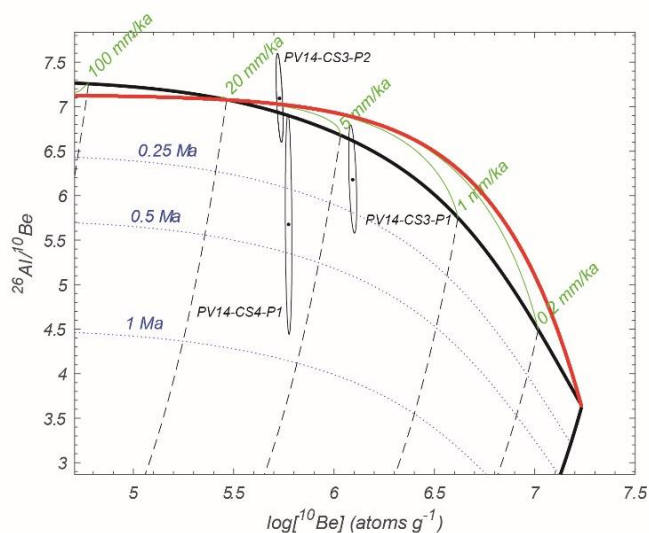
408 Boulders and cobbles of granite, gneiss, Beacon sandstone and dolerite pepper the Pearse
409 Valley floor, forming a thin, patchy drift overlying an older, well-weathered relict drift surface.
410 Some boulders lodged in the relict drift host smaller perched boulders, cobbles, and pebbles
411 on their surfaces, indicating deposition of perched clasts occurred after the most recent
412 retreat of Taylor Glacier (Fig. 4).

413

414 Our surface exposure chronology is based on three granitic cobbles on the northern side of
415 the central valley floor (Table 1, Fig. 2). Two samples (PV14-CS3-P2 and PV14-CS4-P1)



416 yielded minimum zero erosion ^{10}Be exposure ages of 65 ± 4 ka and 74 ± 5 ka (1σ external
417 errors), respectively, whereas the third sample (PV14-CS3-P1) yielded an older age of $158 \pm$
418 11 ka, presumably affected by inheritance (Table 1). The three $^{26}\text{Al}/^{10}\text{Be}$ concentration ratios
419 range from 5.7 to 7.1 and when plotted on ^{10}Be - $^{26}\text{Al}/^{10}\text{Be}$ diagram, largely indicates a simple
420 exposure within their 1σ error ellipses without any prior complex history (Fig. 7). While this
421 assumption of zero erosion makes negligible difference for LGM and younger ages, we
422 evaluate the influence of surface erosion on the exposure ages above using known erosion
423 rates reported from Antarctica and geological evidence from the sites. Bedrock and regolith
424 erosion rates in the Dry Valleys range from 0.1–4 mm/ka (Putkonen et al., 2008;
425 Summerfield et al., 1999). A compiled study across Antarctica showed that granite
426 populations have a mean erosion rate of 0.13 mm/ka, and in the Dry valleys, a max erosion
427 rate of 0.65 mm/ka (Marrero et al., 2018). Applying the max erosion rate (0.65 mm/ka) from
428 granite surfaces in the Dry Valleys, erosion corrected ^{10}Be exposure ages of our granitic
429 cobbles resulted in 174 ± 13 ka (PV14-CS3-P1), 68 ± 5 ka (PV14-CS3-P2) and 77 ± 5 ka
430 (PV14-CS4-P1) (1σ external errors; Table 1). The cobble sample PV14-CS3-P2 displays
431 minimal edge rounding which suggests negligible erosion and is unlikely to be much older
432 than the zero-erosion age.



433

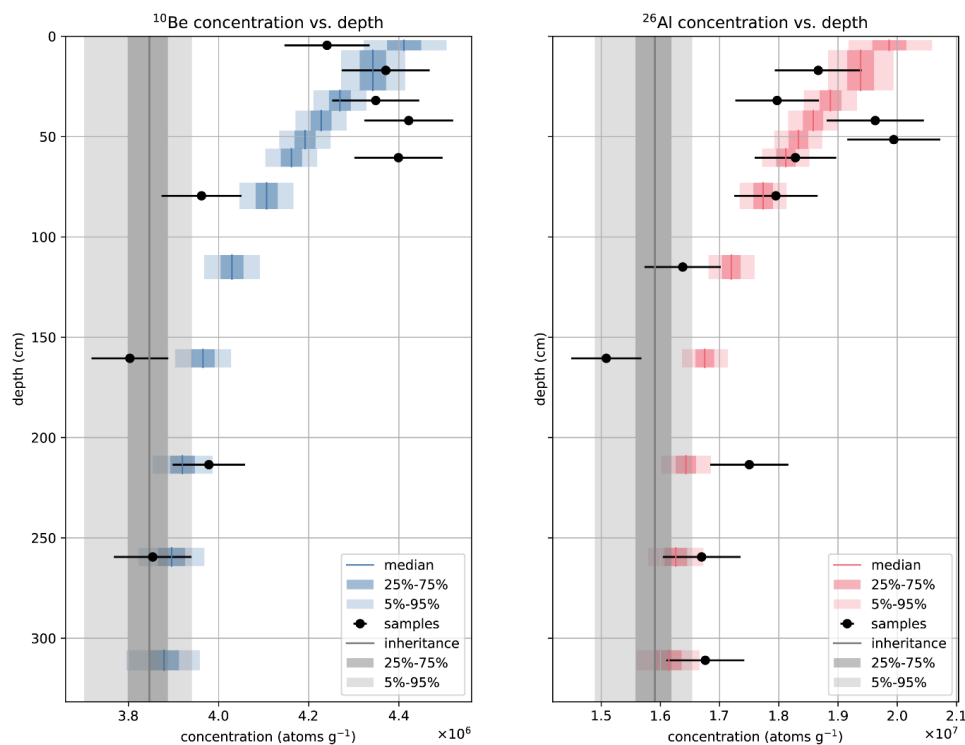
434 **Figure 7.** Two-isotope plot of Pearse Valley cobbles. Nuclide concentrations with 1σ
435 uncertainties, using the time-dependent LSDn scaling scheme of Lifton et al. (2014). Burial
436 isochrons (dotted lines), decay trajectories (dashed), the exposure-erosion region (bounded
437 by black and red lines), and steady-state erosion loci (green) are shown.

438



439 4.2 Cosmogenic nuclide depth profiles at Pearse Valley

440 The ^{10}Be and ^{26}Al depth profiles from the permafrost core and overlying active-layer at
441 Pearse Valley, and associated modelled nuclide concentrations from a best-fit to all samples
442 are shown in Fig. 8. No acceptable depth profile model fit was obtained for all measured ^{10}Be
443 and ^{26}Al depth profile samples (see Fig. 8). However, the model appears to have performed
444 better for the deeper samples >2.09 m, than for the shallower samples <1.65 m. This result
445 suggests that the depth profile is of a composite structure. This is supported by the
446 observation that ice lenses appear at ~ 0.7 m, and at ~ 1.70 – 1.80 m, which are also
447 associated with distinct changes in ^{10}Be and ^{26}Al concentrations. Between 0.65 m and 1.65
448 m, both ^{10}Be and ^{26}Al cosmogenic nuclide concentrations display attenuation with depth,
449 whilst below 1.65 m, the attenuation is interrupted by a considerable increase in nuclide
450 concentrations as shown in the sample at 2.09 m depth. We attempt a model best-fit only to
451 the samples above 1.65 m in order to determine the younger depositional phase. The five
452 ^{10}Be and five ^{26}Al nuclide concentrations from 0.02 – 0.65 m exhibit a uniform concentration
453 with depth with averages of $4.36 \pm 0.10 \times 10^6$ atoms g^{-1} and $1.89 \pm 0.07 \times 10^7$ atoms g^{-1} ,
454 respectively, with no attenuation, indicating that these upper sediments have been vertically
455 mixed (or possibly deposited sufficiently recently so that nuclide depth profiles effectively
456 reflect only inheritance without significant post-depositional production). To accommodate
457 the vertically-mixed, uniform ^{10}Be and ^{26}Al concentrations in the upper 0.65 m we use the
458 mean ^{10}Be and ^{26}Al concentrations from these samples to best represent the process that
459 resulted in the uniform profile (i.e., a vertically mixed cryoturbated layer or the most recent
460 deposition) as shown in Fig. 9. The best-fit modelled nuclide concentrations for the PV14-A
461 depth profile when restricted to samples from 0.02 to 1.65 m depth, falls within the 25th to
462 75th percentile of the measured concentrations. We constrained the erosion rate of the depth
463 profiles using information from surface cobble PV14-CS3-P2 which sits ~ 10 – 20 cm above
464 the desert pavement and has a minimum exposure age of 65 ka (Fig. 4a). Based on this
465 observation we can assume a maximum surface lowering rate of ~ 0.3 cm ka^{-1} . Using this
466 field observation, we applied a conservatively high erosion rate limit of 0.4 cm ka^{-1} for our
467 depth profile modelling. The solutions yield most probable ^{10}Be and ^{26}Al inheritance
468 concentrations of 3.59×10^6 and 1.42×10^7 atoms g^{-1} , respectively (Fig. 9; Fig S1) and
469 constrain the depositional age of the permafrost (<1.65 m depth) at 180^{+20}_{-40} ka (Fig. 10),
470 and an erosion rate of $0.24^{+0.10}_{-0.09}$ cm ka^{-1} (Fig. S2). By inference, the lower part of the
471 profile (>2.09 m depth) predates the sediments above and must be deposited before ~ 180
472 ka.



473

474 **Figure 8.** Pearse Valley (PV14-A) permafrost core depth profiles with measured ^{10}Be and
475 ^{26}Al concentrations (black data points) with 1σ uncertainties for all samples between 0.02–
476 3.16 m depth. Blue (^{10}Be) and red (^{26}Al) boxes show simulated nuclide concentrations at
477 each sample depth.

478

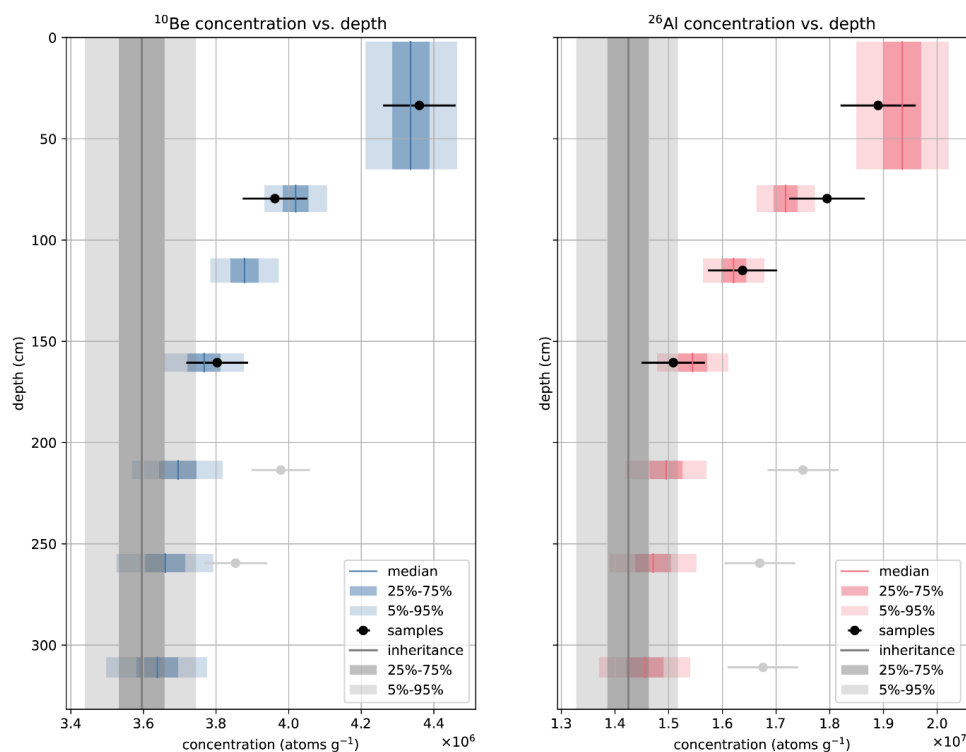
479 4.3 Cosmogenic nuclide depth profiles at Lower Wright Valley

480 The ^{10}Be and ^{26}Al depth profiles from the permafrost core and overlying active-layer used for
481 depth profile modelling at Lower Wright Valley is shown in Fig 11. The Lower Wright Valley
482 ^{10}Be and ^{26}Al concentration profiles exhibit near-constant concentrations with depth with
483 average values of $4.01 \pm 0.10 \times 10^6$ atoms g^{-1} and $2.08 \pm 0.08 \times 10^7$ atoms g^{-1} , respectively.
484 The absence of a discernible exponential attenuation indicates all sediments in the depth
485 profile are either vertically mixed after deposition, or are sufficiently young so that post-
486 depositional nuclide production is negligible relative to inheritance.

487 The depth profile model does not work well for non-attenuating profiles and usually fails to give
488 well-constrained results. The modelled nuclide concentration depth profiles do not fit within the
489 5th to 95th percentile for our measured concentrations in the Lower Wright Valley depth profile
490 (Fig. 11). The solutions yield most probable ^{10}Be and ^{26}Al inheritance concentrations of $4.03 \times$

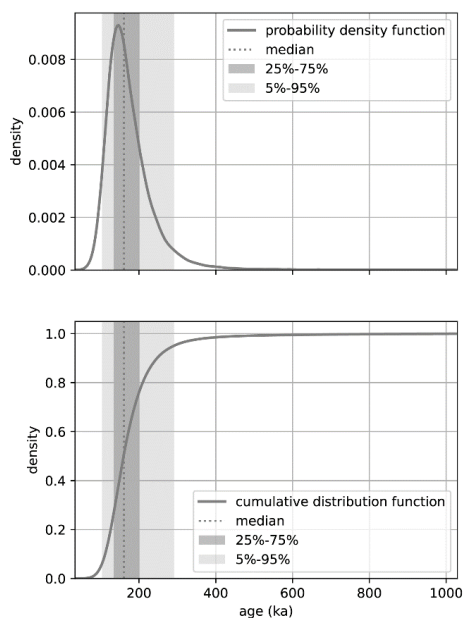


491 10^6 and 2.06×10^7 atoms g^{-1} , respectively (Fig. 11; Fig. S3). Our simulations yield the
492 depositional age of the permafrost at $4.4^{+8.2} / -4.2$ ka (5th to 95th percentile), and an erosion rate
493 of $0.2^{+0.18} / -0.18$ cm ka^{-1} (Fig. S3).



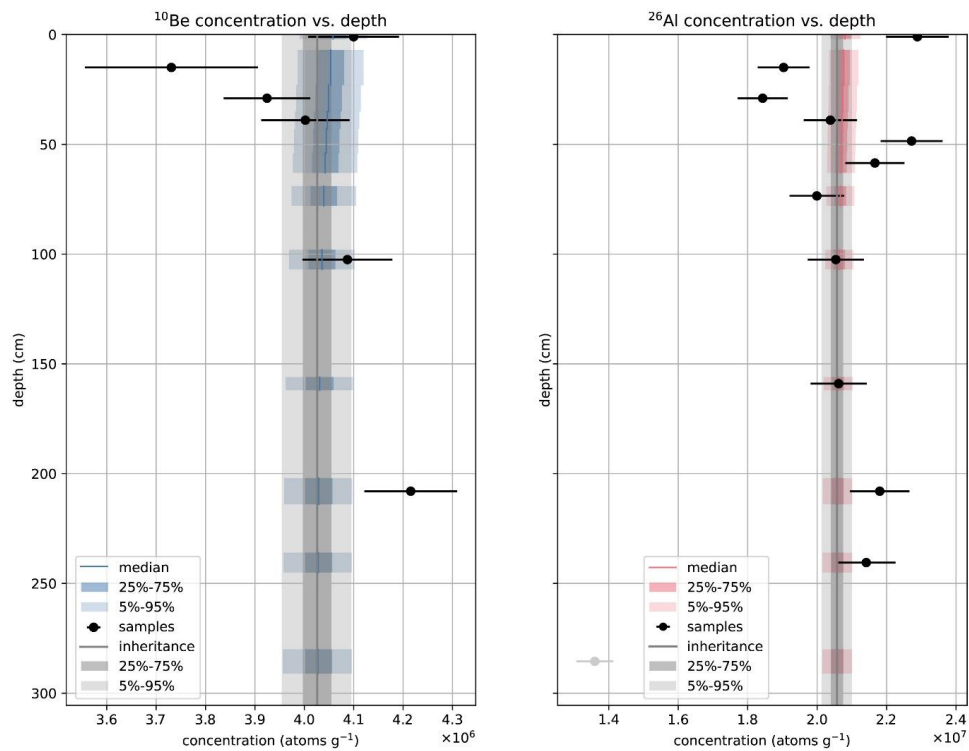
494

495 **Figure 9.** Pearse Valley (PV14-A) permafrost core depth profiles with measured ^{10}Be and
496 ^{26}Al concentrations (black data points) with 1σ uncertainties. For all samples between 0.02–
497 0.65 m depth, we used the average concentration of all five ^{10}Be and ^{26}Al measurements to
498 represent the effect of cryoturbation of sediments in the active-layer. Blue (^{10}Be) and red
499 (^{26}Al) boxes show simulated nuclide concentrations at each depth. ^{10}Be and ^{26}Al
500 concentrations (grey data points) below 2.09 m were not included in the model.



501

502 **Figure 10.** Probability density function, and cumulative distribution function for exposure
 503 age, using dual-nuclide depth profile modelling for PV14-A.



504



505 **Figure 11.** Lower Wright Valley (WV14-l) permafrost core depth profiles with measured ^{10}Be
506 and ^{26}Al concentrations (black data points) with 1σ uncertainties. Blue (^{10}Be) and red (^{26}Al)
507 boxes show simulated nuclide concentrations at each depth.

508

509 **5 Discussion**

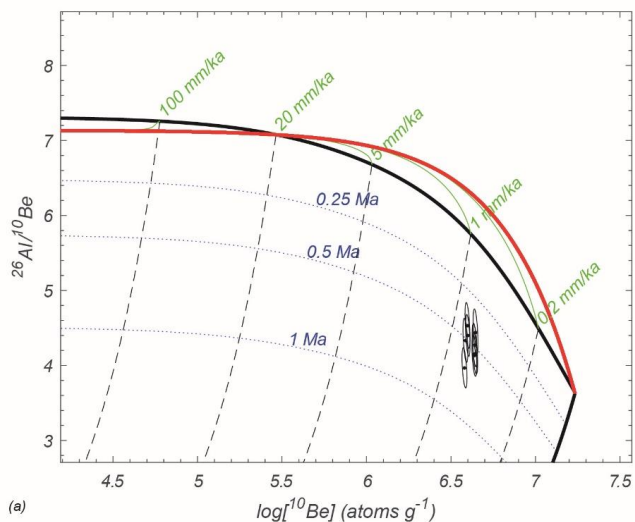
510 **5.1 Depositional and permafrost processes at Pearse Valley**

511 Thin, patchy drift at Pearse Valley is a discontinuous peppering of boulders and cobbles
512 superimposed on older loose sandy sediments, reworked clasts, and underlying permafrost
513 sediments (Fig. 4). Surface cobble exposure ages confirm that this thin, patchy drift was
514 deposited by a retreating cold-based Taylor Glacier during MIS 5a, and the MIS 5 / 4
515 transition, and corresponds with Taylor 2 Drift in central Taylor Valley. Depth profile
516 modelling confirms that the sediments underlying Taylor 2 Drift, predate MIS 5. Undisturbed
517 preservation of these relict surfaces is consistent with cold-based glacier activity described
518 by Atkins (2013).

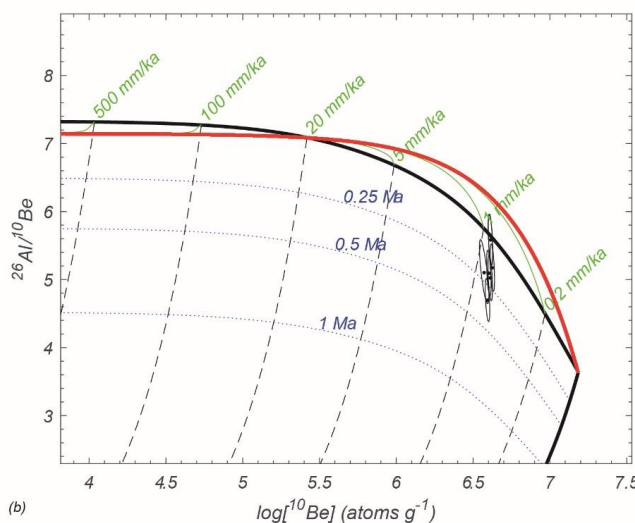
519 At the PV14-A permafrost core site, the present-day active-layer comprises a desert pavement
520 surface and layer of loose vertically mixed sediments to a depth of ~ 0.37 m, positioned above
521 ice-cemented permafrost sediments. The interface between this active-layer and the ice-
522 cemented permafrost represents a sublimation unconformity. However, there is a discernible
523 decrease in ^{10}Be concentration in the permafrost at ~ 0.65 m depth alongside an ice horizon.
524 Such ice horizons are indicative of a paleosublimation unconformity, and the presence of a
525 paleosublimation unconformity suggests the sediments experienced intervals that are warmer
526 than present-day during or after deposition. This ^{10}Be offset cannot be explained by active-layer
527 cryoturbation, as the present-day active-layer is only 0.37 m deep. Lapalme et al. (2017)
528 suggested that in the upper ~ 0.5 m of a soil profile, ice can accumulate and sublimate due to
529 changing ground surface temperature and humidity conditions. Below ~ 0.5 m depth, ice will
530 progressively increase over time. Therefore, a paleosublimation unconformity can be inferred
531 by the increase in ice content from 60 to 40 cm depth, which records the maximum predicted
532 ice table depth (Lapalme et al., 2017). Therefore, we suggest the ^{10}Be offset between the
533 sediments above and below 0.65 m represent a paleosublimation unconformity (Fig. 5a, 8)
534 which probably occurred when the active-layer was thicker than present. Our depth profile
535 model indicates that the upper section of the Pease Valley permafrost sediments (< 1.65 m)
536 was likely deposited at $180^{+20} / -40$ ka, which does not contradict the exposure ages of the thin,
537 patchy drift ($\sim 65\text{--}74$ ka). Our measured nuclide concentrations at > 2.09 m depth largely differ
538 from the upper section and do not fit the simulated depth profile (Fig. 9). The higher nuclide
539 concentrations in these samples, alongside the presence of several small ice lenses between



540 1.57–1.87 m depth suggest these sediments were deposited during an earlier depositional
541 event before ~180 ka.



(a)



(b)

542

543 **Figure 12.** Two-isotope plot of Pearse Valley (a) and Lower Wright Valley (b) depth profiles.
544 Nuclide concentrations with 1σ uncertainties, using the time-dependent LSDn scaling
545 scheme of Lifton et al. (2014). Burial isochrons (dotted lines), decay trajectories (dashed),
546 the exposure-erosion region (bounded by black and red lines), and steady-state erosion loci
547 (green) are shown.

548

549 **5.2 Exposure-burial history of sediments in Pearse Valley and Lower Wright Valley**



550 While nuclide depth profiles indicate the most recent depositional history of the permafrost
551 sediment, $^{26}\text{Al}/^{10}\text{Be}$ ratio data provides an additional insight regarding the total history of the
552 sediment. When $^{26}\text{Al}/^{10}\text{Be}$ is plotted against ^{10}Be concentration on a two-isotope diagram
553 (Fig. 12), a minimum total exposure-burial period can be inferred on the assumption that the
554 sample experienced only one cycle of continuous exposure followed by continuous deep
555 burial. At the Pearse Valley site, the two-isotope plot indicates that all sediments, regardless
556 of their depth, have $^{26}\text{Al}/^{10}\text{Be}$ ratios ranging from 3.97 to 4.53, resulting in a minimum ~800
557 ka simple exposure (at zero erosion), and minimum ~400 ka burial, with a total exposure
558 history of at least 1.2 Ma. At the Lower Wright Valley site, $^{26}\text{Al}/^{10}\text{Be}$ ratios for all samples
559 range from 4.70 to 5.58, resulting in a minimum ~900 ka simple exposure, and minimum
560 ~300 ka burial, with a total exposure history of at least 1.2 Ma.

561 Depth profile ages at both permafrost core sites represent the most recent phase of their
562 depositional histories. For Pearse Valley this occurred at ~180 ka, and for Lower Wright Valley,
563 where ^{10}Be and ^{26}Al concentrations do not attenuate, we estimate a maximum deposition age
564 of <25 ka. This age represents the time required to change ^{10}Be and ^{26}Al above the initial
565 inheritance level for near-surface samples by 5% - a change outside AMS ^{10}Be and ^{26}Al
566 measurement error. However, our $^{26}\text{Al}/^{10}\text{Be}$ ratios at both sites suggest that these sediments
567 have much longer total exposure-burial histories of at least 1.2 Ma, which most likely involves
568 multiple recycling episodes of exposure, deposition, burial, and deflation prior to deposition at
569 their current locations. Million-year exposure-burial recycling periods of sediments in the Dry
570 Valleys was also observed in shallow (<1 m) pits from the Packard Dune fields in Victoria Valley
571 (Fink et al., 2015).

572

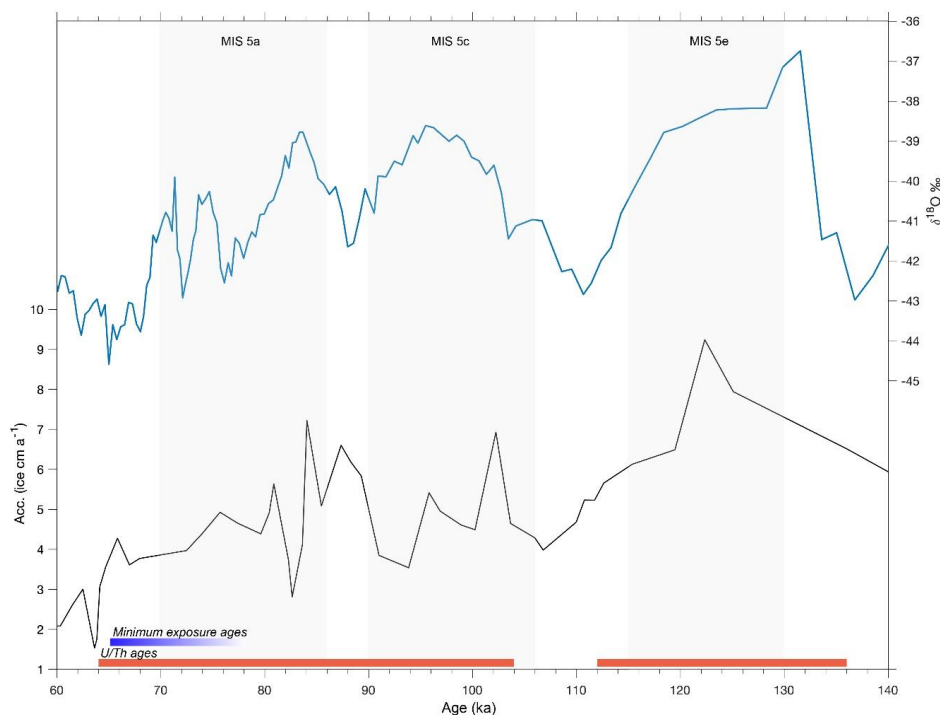
573 **5.3 Fluctuations of Taylor Glacier in Pearse Valley during MIS 5**

574 Surface exposure ages of the cobbles perched on large boulders together with constraints
575 from a best-fit depth profile age indicate Taylor 2 Drift sediments were deposited ~65–74 ka,
576 during MIS 5a, and the MIS 5 / 4 transition, on the northern valley floor of central Pearse
577 Valley, whereas the underlying permafrost sediments were deposited at ~180 ka or earlier.
578 Our surface cobble geochronology is in agreement with the minimum U/Th ages for the extent
579 of proglacial Lake Bonney, which suggest retreat of Taylor Glacier following MIS 5c and 5a
580 advance (Fig. 13; Higgins et al., 2000a), and the tentatively dated western section of the rock
581 glacier derived from $\delta^{18}\text{O}$ in buried ice northern Pearse Valley (Swanger et al., 2019). These
582 data suggest Pearse Valley was largely or partially glaciated throughout MIS 5c and 5a.

583 Retreat of the Taylor Glacier lobe in Pearse Valley possibly continued after 65 ka. Timing of
584 retreat after 65 ka, until the Last Glacial Maximum, where Taylor Glacier was at a minimum



585 position, remains unknown. Advance and retreat cycles during MIS 5, the final retreat of Taylor
586 Glacier during MIS 5a, and between the MIS 5 / 4 transition and the LGM for Taylor Glacier,
587 could be better constrained by exposure dating more drift deposits with larger spatial coverage
588 from Pearse Valley.



589
590 **Figure 13.** Snow accumulation rate determined from ^{10}Be (Acc. (ice cm a^{-1})) and $\delta^{18}\text{O}$ record
591 from Taylor Dome during MIS 5 (Steig et al., 2000). U/Th ages from algal carbonates (red
592 bands, Higgins et al., 2000a) coincide with warm MIS substages 5e, 5c and 5a with
593 increased accumulation rates at Taylor Dome. This is consistent with our minimum exposure
594 ages (blue band) which show retreat of Taylor Glacier in Pearse Valley during MIS 5a, and
595 the MIS 5 / 4 transition.

596

597 **5.4 Advance and retreat of outlet and alpine glaciers during interglacial periods**

598 Our new data has implications regarding the relationship between outlet and alpine glacier
599 behaviour, regional paleoclimate and the extent of sea ice and open ocean conditions in the
600 Ross Sea. Snow accumulation rate, atmospheric temperature, and duration of precipitation
601 appear to be the major controls governing the advance and retreat of Taylor Glacier during
602 previous warm intervals (Fig. 13). In central Taylor Valley, substage 5a and 5c sediments
603 bury 5e sediments suggesting Taylor Glacier responds to regional changes over millennial



604 timescales (Higgins et al., 2000a). The Taylor Glacier advances in central Taylor Valley
605 during substages 5e, 5c and 5a correspond with increased accumulation in Taylor Dome
606 (Higgins et al., 2000a; Steig et al., 2000). Our exposure ages indicate the retreat of Taylor
607 Glacier in Pearse Valley occurred at ~65–74 ka during the MIS 5 / 4 transition, and is
608 consistent with the retreat in central Taylor Valley. The presence of a lobe of Taylor Glacier
609 in Pearse Valley throughout MIS 5 is likely linked to prolonged interglacial climate conditions.
610 The interglacial-mode climate, where austral westerlies are in a poleward-shifted position for
611 prolonged periods during MIS 5, is associated with periods where CO₂ concentrations were
612 above ~230 ppm, the glacial-interglacial CO₂ threshold proposed by Denton et al. (2021).

613 Yan et al. (2021) suggested that peak accumulation rates occurred at ~128 ka in Southern
614 Victoria Land and are associated with reduced sea ice and possibly retreat of the Ross Ice
615 Shelf. The study suggested by ~125 ka, the Ross Ice Shelf had returned to a configuration
616 comparable to present day. However, a reduction of sea ice may have enabled increased
617 moisture delivery over Taylor Dome during MIS 5c and 5a. As Higgins et al. (2000a)
618 suggested, increased precipitation over Taylor Dome during MIS 5a and 5c appears to have
619 caused a subsequent readvance of Taylor Glacier. We acknowledge, this hypothesis is
620 speculative and requires further testing of temperature, and atmospheric circulation in
621 response to reduced sea ice extent and perhaps a reduction of the Ross Ice Shelf by climate
622 models.

623 The duration of a warm interval which governs the extent of sea ice cover or open water in
624 the Ross Sea, may in turn, influence moisture transport and accumulation on Taylor Dome
625 and the Antarctic plateau. With temperatures predicted to be similar to the last interglacial in
626 coming decades, on a multicentennial to millennial scale, anti-phased MIS 5 feedbacks may
627 provide important analogues for future Antarctic ice loss (DeConto & Pollard, 2016; DeConto
628 et al., 2021). While our geochronology suggests retreat of Taylor Glacier in Pearse Valley
629 occurred during the MIS 5 / 4 transition, probably by a change in moisture regime and drying
630 during MIS 5a, several uncertainties regarding advancing and retreating ice and associated
631 processes in the Dry Valleys region and Ross Sea need to be addressed:

- 632 • The timing of advance and retreat cycles of outlet and alpine glaciers during
633 substages 5e, 5c and 5a remain poorly constrained.
- 634 • The duration of warm intervals, bringing warm moist air to enable glacier advance is
635 not well understood.
- 636 • The paucity of data in the Ross Sea regarding sea ice, ice shelf, and open ocean
637 conditions during MIS 5 makes interpretation of the antiphase behaviour between
638 advanced outlet and alpine glaciers in the Dry Valleys region, and increased open



639 ocean in the Ross Sea difficult to quantify.

640

641 **6 Conclusions**

642 We applied cosmogenic nuclide analysis to surface cobbles and permafrost depth profiles to
643 obtain the age of Taylor 2 Drift, and determine landscape evolution and associated
644 processes in Pearse Valley. Our ^{10}Be and ^{26}Al derived surface exposure ages from cobbles
645 emplaced on large boulders embedded in the valley floor of Pearse Valley located ~3 km
646 from Taylor Glacier lobe give a minimum zero erosion age of ~65 to 74 ka for deposition of
647 the thin, patchy drift, indicating that Taylor Glacier retreated from Pearse Valley during MIS 5
648 / 4 transition. Companion ^{10}Be and ^{26}Al depth profile modelling reveals a ~180 ka deposition
649 age for near-surface permafrost deposits to 1.65 m depth that predates MIS 5. These data
650 support antiphase behaviour between outlet and alpine glaciers in the Dry Valleys region
651 and ice extent in the Ross Sea, and suggest a causal mechanism where cold-based glacier
652 advance and retreat is controlled by moisture availability and drying, respectively due to ice
653 retreat and expansion in the Ross Sea. Our work is consistent with geochronology from
654 central Taylor Valley, supporting advance and retreat cycles of Taylor Glacier during MIS
655 substages 5c and 5a (Higgins et al., 2000a), corresponding with increased accumulation at
656 Taylor Dome (Steig et al. 2000). Our study highlights the need for better age constraints of
657 alpine and outlet glaciers that advanced during MIS 5 in the Dry Valley region. In particular,
658 for assessing the relationship between accumulation rate at Taylor Dome, and sea ice, ice
659 shelf, and open ocean conditions in the Ross Sea during MIS 5.

660 The offset in ^{10}Be concentrations at ~0.65 m depth in the Pearse Valley permafrost core, and
661 presence of increased ice content reveals a paleosublimation unconformity, and suggests
662 that these upper sediments have undergone active-layer cryoturbation. The permafrost
663 >0.65 m depth in central Pearse Valley has been frozen for at least 65 ka, and perhaps ~180
664 ka based on our depth profile model, whereas, >2.09 m depth the depositional age of the
665 sediment must be earlier than ~180 ka.

666 To compare processes of sediment evolution at Pearse Valley with a lower elevation, and
667 more coastal environment, we also applied ^{10}Be and ^{26}Al nuclide analysis to permafrost
668 depth profiles at Lower Wright Valley. While the current deposition at the latter site occurred
669 more recently (<25 ka), total exposure-burial histories from the two sites consistently show
670 these sediment repositories have experienced multiple glacial-interglacial cycles achieved
671 through the recycling of sediments for at least 1.2 Ma.

672



673 **Code availability**

674 The code used for depth profile modelling is available by request from the corresponding
675 author.

676 **Data availability**

677 All data described in the paper are included in the Supplement.

678 **Author contributions**

679 JTHA, GSW, AA, and ND conducted the field work and sample collection. JTHA, DF, TF,
680 and KW conducted the sample preparation and AMS analysis. AJH and JTHA developed the
681 depth profile models. JTHA prepared the manuscript with contributions from all authors.

682 **Competing interests**

683 The authors declare that they have no conflict of interest.

684 **Acknowledgements**

685 We thank Craig Cary, Ian McDonald, Bob Dagg and Steph Lambie for assistance in the field,
686 Antarctica New Zealand and Southern Lakes Helicopters for logistical support, and Steve
687 Kotevski for laboratory assistance.

688 **Financial Support**

689 This research was supported by NZARI (RFP 2014-1), and ANSTO Portal grants 12215 and
690 12260 and an AINSE Postgraduate Research Award. JTHA was supported by a Sir Robin
691 Irvine Scholarship, and a University of Otago departmental award. AA and ND were partially
692 supported by the Russian Antarctic Expedition. We acknowledge the financial support from
693 the Australian Government for the Centre for Accelerator Science at ANSTO through the
694 National Collaborative Research Infrastructure Strategy (NCRIS). Prepared in part by LLNL
695 under Contract DE-AC52-07NA27344; LDRD grant 19-LW-036. This is LLNL-JRNL-842669.

696

697 **References**

- 698 Anderson, R. S., Repka, J. L., & Dick, G. S. (1996). Explicit treatment of inheritance in
699 dating depositional surfaces using in situ ^{10}Be and ^{26}Al . *Geology*, 24(1), 47–51.
700 [https://doi.org/10.1130/0091-7613\(1996\)024<0047:ETOIID>2.3.CO;2](https://doi.org/10.1130/0091-7613(1996)024<0047:ETOIID>2.3.CO;2)
- 701 Atkins, C. (2013). Geomorphological evidence of cold-based glacier activity in South Victoria
702 Land, Antarctica. *Geological Society, London, Special Publications*.
703 <https://doi.org/10.1144/SP381.18>
- 704 Balco, G, Stone, J. O., Lifton, N. A., & Dunai, T. J. (2008). A complete and easily accessible



- 705 means of calculating surface exposure ages or erosion rates from ^{10}Be and ^{26}Al
706 measurements. *Quaternary Geochronology*, 3(3), 174–195.
707 <https://doi.org/10.1016/j.quageo.2007.12.001>
- 708 Balco, G. (2017). Production rate calculations for cosmic-ray-muon-produced ^{10}Be and ^{26}Al
709 benchmarked against geological calibration data. *Quaternary Geochronology*, 39, 150–
710 173. <https://doi.org/10.1016/j.quageo.2017.02.001>
- 711 Bergelin, M., Putkonen, J., Balco, G., Morgan, D., Corbett, L. B., & Bierman, P. R. (2022).
712 Cosmogenic nuclide dating of two stacked ice masses : Ong Valley, Antarctica. *The*
713 *Cryosphere*, 16(7), 2793-2817. <https://doi.org/10.5194/tc-16-2793-2022>
- 714 Bibby, T., Putkonen, J., Morgan, D., Balco, G., & Shuster, D. L. (2016). Million year old ice
715 found under meter thick debris layer in Antarctica. *Geophysical Research Letters*,
716 43(13), 6995–7001. <https://doi.org/10.1002/2016GL069889>
- 717 Blackburn, T., Edwards, G. H., Tulaczyk, S., Scudder, M., Piccione, G., Hallet, B., McLean,
718 N., Zachos, J.C., Cheney, B., & Babbe, J. T. (2020). Ice retreat in Wilkes Basin of East
719 Antarctica during a warm interglacial. *Nature*, 583(7817), 554–559.
720 <https://doi.org/10.1038/s41586-020-2484-5>
- 721 Bockheim, J.G.; Campbell, I.G., McCleod, M. (2007). Permafrost Distribution and Active-Layer
722 Depths in the McMurdo Dry Valleys, Antarctica. *Permafrost and Periglac. Process.*,
723 18(3), 217–227. <https://doi.org/10.1002/ppp.588>
- 724 Bockheim, A. J. G., Prentice, M. L., & Mcleod, M. (2008). Distribution of Glacial Deposits,
725 Soils, and Permafrost in Taylor Valley, Antarctica. *Arctic, Antarctic, and Alpine*
726 *Research*, 40(2), 279–286. [https://doi.org/10.1657/1523-0430\(06-057\)](https://doi.org/10.1657/1523-0430(06-057))
- 727 Borchers, B., Marrero, S., Balco, G., Caffee, M., Goehring, B., Lifton, N., Nishiizumi, K.,
728 Phillips, F., Schaefer, J., & Stone, J. (2016). Geological calibration of spallation
729 production rates in the CRONUS-Earth project. *Quaternary Geochronology*, 31, 188–
730 198. <https://doi.org/10.1016/j.quageo.2015.01.009> Brook, E. J., Kurz, M. D., Ackert, R.
731 P., Denton, G. H., Brown, E. T., Raisbeck, G. M., & Yiou, F. (1993). Chronology of
732 Taylor Glacier advances in Arena Valley, Antarctica, using in situ cosmogenic ^3He and
733 ^{10}Be . *Quaternary Research*, 39(1), 11-23. <https://doi.org/10.1006/qres.1993.1002>
- 734 Child, D., Elliott, G., Mifsud, C., Smith, A. M., & Fink, D. (2000). Sample processing for earth
735 science studies at ANTARES. *Nuclear Instruments and Methods in Physics Research,*
736 *Section B: Beam Interactions with Materials and Atoms*, 172(1–4), 856–860.
737 [https://doi.org/10.1016/S0168-583X\(00\)00198-1](https://doi.org/10.1016/S0168-583X(00)00198-1)
- 738 Chorley, H., Levy, R., Naish, T., Lewis, A., Cox, S., Hemming, S., Ohneiser C, Gorman A,
739 Harper M, Homes A, Hopkins J., Prebble, J., Verret, M., Dickinson, W., Florindo, F.,
740 Golledge, N., Halberstadt, A. R., Kowalewski, D., McKay, R., Meyers, S., Anderson, J.,
741 Dagg, B., & Lurcock, P. (2022). East Antarctic Ice Sheet variability during the middle
742 Miocene Climate Transition captured in drill cores from the Friis Hills, Transantarctic
743 Mountains. *GSA Bulletin*. <https://doi.org/10.1130/B36531.1>
- 744 Cook, C. P., Van De Fliedrt, T., Williams, T., *et al.* (2013). Dynamic behaviour of the East
745 Antarctic ice sheet during Pliocene warmth. *Nature Geoscience*, 6(9), 765–769.
746 <https://doi.org/10.1038/ngeo1889> Cox, S. C., Turnbull, I. M., Isaac, M. J., Townsend, D.
747 B., & Smith Lyttle, B. (2012). *Geology of Southern Victoria Land, Antarctica. Institute of*
748 *geological & Nuclear Sciences 1:25,000 geological map 22. 135 p. + 1 folded map.*
749 Lower Hutt, New Zealand. GNS Science.
- 750 Davis, T. N. (2001). *Permafrost: A Guide to Frozen Ground in Transition*. Fairbanks, AK:
751 University of Alaska Press. 351 pp. ISBN 1-889963-19-4. *Journal of*
752 *Glaciology*, 48(162), 478-478. <https://doi.org/10.3189/172756502781831223>



- 753 DeConto, R. M., & Pollard, D. (2016). Contribution of Antarctica to past and future sea-level
754 rise. *Nature*, 531(7596), 591–597. <https://doi.org/10.1038/nature17145>
- 755 DeConto, R. M., Pollard, D., Alley, R. B., Velicogna, I., Gasson, E., Gomez, N., Sadai, S.,
756 Condrón, A., Gilford, D. M., Ashe, E. L., Kopp R. E., Li, D., & Dutton, A. (2021). The
757 Paris Climate Agreement and future sea-level rise from Antarctica. *Nature*, 593(7857),
758 83–89. <https://doi.org/10.1038/s41586-021-03427-0>
- 759 Denton, G.H., Armstrong R.L., & Stuiver, M. (1970). Late Cenozoic Glaciation in Antarctica:
760 The Record in the McMurdo Sound Region. *Antarctic Journal of the United States*, 5(1),
761 15–21.
- 762 Denton, G. H., Putnam, A. E., Russell, J. L., Barrell, D. J. A., Schaefer, J. M., Kaplan, M. R.,
763 & Strand, P. D. (2021). The Zealandia Switch: Ice age climate shifts viewed from
764 Southern Hemisphere moraines. *Quaternary Science Reviews*, 257, 106771.
765 <https://doi.org/10.1016/j.quascirev.2020.106771>
- 766 Doran, P. T., McKay, C. P., Clow, G. D., Dana, G. L., Fountain, A. G., Nysten, T., & Lyons, W.
767 B. (2002). Valley floor climate observations from the McMurdo dry valleys, Antarctica,
768 1986-2000. *Journal of Geophysical Research Atmospheres*, 107(24), ACL 13-1-ACL
769 13-12. <https://doi.org/10.1029/2001JD002045>
- 770 Dutton, A., Carlson, A. E., Long, A. J., Milne, G. A., Clark, P. U., DeConto, R., Horton, B.,
771 Rahmstorf, S., & Raymo, M. E. (2015). Sea-level rise due to polar ice-sheet mass loss
772 during past warm periods. *Science*, 349(6244). <https://doi.org/10.1126/science.aaa4019>
- 773 Dutton, A., & Lambeck, K. (2012). Ice volume and sea level during the last interglacial.
774 *Science*, 337(6091), 216–219. <https://doi.org/10.1126/science.1205749>
- 775 Fink, D., Augustinus, P., Rhodes, E., Bristow, C., & Balco, G. (2015). 21Ne, 10Be and 26Al
776 cosmogenic burial ages of near-surface eolian sand from the Packard Dune field,
777 McMurdo Dry Valleys, Antarctica. *EGU General Assembly Vol. 17*.
778 2015EGUGA..17.2922F
- 779 Fischer, H., Meissner, K. J., Mix, A. C., Abram, N. J., Austermann, J., Brovkin, V., *et al.*
780 (2018). Palaeoclimate constraints on the impact of 2 °c anthropogenic warming and
781 beyond. *Nature Geoscience*, 11(7), 474–485. [https://doi.org/10.1038/s41561-018-0146-](https://doi.org/10.1038/s41561-018-0146-0)
782 0
- 783 Fountain, A. G., Nysten, T. H., Monaghan, A., Basagic, H. J., & Bromwich, D. (2010). Snow in
784 the Mcmurdo Dry Valleys, Antarctica. *International Journal of Climatology*, 30(5), 633–
785 642. <https://doi.org/10.1002/joc.1933>
- 786 French, H. M. (2017). *The periglacial environment*. Wiley-Blackwell (4th ed.). John Wiley &
787 Sons.
- 788 Gollledge, N. R., Clark, P. U., He, F., Dutton, A., Turney, C. S. M., Fogwill, C. J., Naish, T.R.,
789 Levy, R.H., McKay, R.M., Lowry, D.P., Bertler, N.A., Dunbar, G. B., & Carlson, A. E.
790 (2021). Retreat of the Antarctic Ice Sheet During the Last Interglaciation and
791 Implications for Future Change. *Geophysical Research Letters*, 48(17), 1–11.
792 <https://doi.org/10.1029/2021GL094513>
- 793 Gunn, B. M., & Warren, G. (1962). *Geology of Victoria Land between the Mawson and*
794 *Mulock Glaciers, Antarctica*. New Zealand Dept. of Scientific and Industrial Research.
- 795 Hall, B. L., Denton, G. H., & Overturf, B. (2001). Glacial Lake Wright, a high-level antarctic
796 lake during the LGM and early holocene. *Antarctic Science*, 13(1), 53–60.
797 <https://doi.org/10.1017/S0954102001000086>
- 798 Hall, B. L., & Denton, G. H. (2005). Surficial geology and geomorphology of eastern and



- 799 central Wright Valley, Antarctica. *Geomorphology*, 64(1–2), 25–65.
800 <https://doi.org/10.1016/j.geomorph.2004.05.002>
- 801 Heldmann, J. L., Marinova, M., Williams, K. E., Lacelle, D., McKay, C. P., Davila, A., Pollard,
802 W., & Andersen, D. T. (2012). Formation and evolution of buried snowpack deposits in
803 Pearse Valley, Antarctica, and implications for Mars. *Antarctic Science*, 24(3), 299–316.
804 <https://doi.org/10.1017/S0954102011000903>
- 805 Hidy, A. J., Gosse, J. C., Pederson, J. L., Mattern, J. P., & Finkel, R. C. (2010). A
806 geologically constrained Monte Carlo approach to modeling exposure ages from
807 profiles of cosmogenic nuclides: An example from Lees Ferry, Arizona. *Geochemistry,*
808 *Geophysics, Geosystems*, 11(9). <https://doi.org/10.1029/2010GC003084>
- 809 Hidy, A. J., Gosse, J. C., Sanborn, P., & Froese, D. G. (2018). Age-erosion constraints on an
810 Early Pleistocene paleosol in Yukon, Canada, with profiles of ¹⁰Be and ²⁶Al: Evidence
811 for a significant loess cover effect on cosmogenic nuclide production rates. *Catena*,
812 165(January), 260–271. <https://doi.org/10.1016/j.catena.2018.02.009>
- 813 Higgins, S.M., Denton, G. H., & Hendy, C. H. (2000). Glacial Geomorphology of Bonney
814 Drift, Taylor Valley, Antarctica. *Geografiska Annaler, Series A: Physical Geography*,
815 82A(2&3), 365–389. <https://doi.org/10.1111/1468-0459.00129>
- 816 Higgins, Sean M., Hendy, C. H., & Denton, G. H. (2000). Geochronology of Bonney Drift,
817 Taylor Valley, Antarctica: Evidence for interglacial expansions of Taylor Glacier.
818 *Geografiska Annaler, Series A: Physical Geography*, 82(2–3), 391–409.
819 <https://doi.org/10.1111/j.0435-3676.2000.00130.x>
- 820 IPCC. (2021). Climate Change 2021. *The Physical Science Basis. Contribution of Working*
821 *Group 1 to Sixth Assessment Report of the Intergovernmental Panel on Climate*
822 *Change*, In Press. Retrieved from <https://www.ipcc.ch/report/ar6/wg1/>
- 823 Jouzel, J., Masson-Delmotte, V., & Cattani, O., Dreyfus G, Falourd S, Hoffmann G, Minster
824 B, Nouet J, Barnola JM, Chappellaz J, Fischer H., *et al.* (2007). Orbital and millennial
825 Antarctic climate variability over the past 800,000 years. *Science*, 317(5839), 793-796.
826 <http://doi.org/10.1126/science.11410>
- 827 Joy, K., Fink, D., Storey, B., De Pascale, G. P., Quigley, M., & Fujioka, T. (2017).
828 Cosmogenic evidence for limited local LGM glacial expansion, Denton Hills, Antarctica.
829 *Quaternary Science Reviews*, 178, 89–101.
830 <https://doi.org/10.1016/j.quascirev.2017.11.002>
- 831 Kopp, R. E., Simons, F. J., Mitrovica, J. X., Maloof, A. C., & Oppenheimer, M. (2009).
832 Probabilistic assessment of sea level during the last interglacial stage. *Nature*,
833 462(7275), 863–867. <https://doi.org/10.1038/nature08686>
- 834 Lapalme, C. M., Lacelle, D., Pollard, W., Fortier, D., Davila, A., & McKay, C. P. (2017).
835 Cryostratigraphy and the Sublimation Unconformity in Permafrost from an Ultraxerous
836 Environment, University Valley, McMurdo Dry Valleys of Antarctica. *Permafrost and*
837 *Periglacial Processes*, 28(4), 649–662. <https://doi.org/10.1002/ppp.1948>
- 838 Lee, J. E., Brook, E. J., Bertler, N. A. N., Buizert, C., Baisden, T., Blunier, T., Ciobanu, V. G.,
839 Conway, H., Dahl-Jensen, D., Fudge, T. J., Hindmarsh, R., Keller, E. D., Parrenin, F.,
840 Severinghaus, J. P., Vallenga, P., Waddington, E. D., & Winstrup, M. (2020). An 83
841 000-year-old ice core from Roosevelt Island, Ross Sea, Antarctica. *Climate of the Past*,
842 16(5), 1691–1713. <https://doi.org/10.5194/cp-16-1691-2020>
- 843 Lewis, A. R., & Ashworth, A. C. (2016). An early to middle Miocene record of ice-sheet and
844 landscape evolution from the Friis Hills, Antarctica. *Geological Society of America*
845 *Bulletin*, 128(5–6), 719–738. <https://doi.org/10.1130/b31319.1>



- 846 Lifton, N., Sato, T., & Dunai, T. J. (2014). Scaling in situ cosmogenic nuclide production
847 rates using analytical approximations to atmospheric cosmic-ray fluxes. *Earth and*
848 *Planetary Science Letters*, 386, 149–160. <https://doi.org/10.1016/j.epsl.2013.10.052>
- 849 Marchant, D. R., Denton, G. H., Bockheim, J. G., Wilson, S. C., & Kerr, A. R. (1994).
850 Quaternary changes in level of the upper Taylor Glacier, Antarctica: implications for
851 paleoclimate and East Antarctic Ice Sheet dynamics. *Boreas*, 23(1), 29–43.
852 <https://doi.org/10.1111/j.1502-3885.1994.tb00583.x>
- 853 Marchant, D. R., Mackay, S. L., Lamp, J. L., Hayden, A. T., & Head, J. W. (2013). A review
854 of geomorphic processes and landforms in the Dry Valleys of southern Victoria Land:
855 Implications for evaluating climate change and ice-sheet stability. *Geological Society*
856 *Special Publication*, 381(1), 319–352. <https://doi.org/10.1144/SP381.10>
- 857 Marchant, D. R., & Denton, G. H. (1996). Miocene and Pliocene paleoclimate of the Dry
858 Valleys region, Southern Victoria land: A geomorphological approach. *Marine*
859 *Micropaleontology*, 27(1–4), 253–271. [https://doi.org/10.1016/0377-8398\(95\)00065-8](https://doi.org/10.1016/0377-8398(95)00065-8)
- 860 Marchant, D. R., & Head, J. W. (2007). Antarctic dry valleys: Microclimate zonation, variable
861 geomorphic processes, and implications for assessing climate change on Mars. *Icarus*,
862 192(1), 187–222. <https://doi.org/10.1016/j.icarus.2007.06.018>
- 863 Marrero, S. M., Hein, A. S., Naylor, M., Attal, M., Shanks, R., Winter, K., Woodward, J.,
864 Dunning, S., Westoby, M. & Sugden, D. (2018). Controls on subaerial erosion rates in
865 Antarctica. *Earth and Planetary Science Letters*, 501, 56–66.
866 <https://doi.org/10.1016/j.epsl.2018.08.018>
- 867 Mercader, J., Gosse, J. C., Bennett, T., Hidy, A. J., & Rood, D. H. (2012). Cosmogenic
868 nuclide age constraints on Middle Stone Age lithics from Niassa, Mozambique.
869 *Quaternary Science Reviews*, 47, 116–130.
870 <https://doi.org/10.1016/j.quascirev.2012.05.018>
- 871 Mifsud, C., Fujioka, T., & Fink, D. (2013). Extraction and purification of quartz in rock using
872 hot phosphoric acid for in situ cosmogenic exposure dating. *Nuclear Instruments and*
873 *Methods in Physics Research Section B: Beam Interactions with Materials and Atoms*,
874 294, 203–207. <https://doi.org/10.1016/j.nimb.2012.08.037>
- 875 Morgan, D. J., Putkonen, J., Balco, G., & Stone, J. (2011). Degradation of glacial deposits
876 quantified with cosmogenic nuclides, Quartermain Mountains, Antarctica. *Earth Surface*
877 *Processes and Landforms*, 36(2), 217–228. <https://doi.org/10.1002/esp.2039>
- 878 Morgan, D., Putkonen, J., Balco, G., & Stone, J. (2010). Quantifying regolith erosion rates
879 with cosmogenic nuclides ^{10}Be and ^{26}Al in the McMurdo Dry Valleys, Antarctica.
880 *Journal of Geophysical Research: Earth Surface*, 115(3), 1–17.
881 <https://doi.org/10.1029/2009JF001443>
- 882 Naish, T., Powell, R., Levy, R., Wilson, G., Scherer, R., Talarico, F., *et al.* (2009). Obliquity-
883 paced Pliocene West Antarctic ice sheet oscillations. *Nature*, 458(7236), 322–328.
884 <https://doi.org/10.1038/nature07867>
- 885 Ng, F., Hallet, B., Sletten, R. S., & Stone, J. O. (2005). Fast-growing till over ancient ice in
886 Beacon Valley, Antarctica. *Geology*, 33(2), 121–124. <https://doi.org/10.1130/G21064.1>
- 887 Nishiizumi, K. (2004). Preparation of ^{26}Al AMS standards. *Nuclear Instruments and Methods*
888 *in Physics Research Section B: Beam Interactions with Materials and Atoms*, 223–224,
889 388–392. <https://doi.org/10.1016/j.nimb.2004.04.075>
- 890 Nishiizumi, K., Imamura, M., Caffee, M. W., Southon, J. R., Finkel, R. C., & McAninch, J.
891 (2007). Absolute calibration of ^{10}Be AMS standards. *Nuclear Instruments and Methods*



- 892 *in Physics Research Section B: Beam Interactions with Materials and Atoms*, 258(2),
893 403–413. <https://doi.org/10.1016/j.nimb.2007.01.297>
- 894 Otto-Bliesner, B. L., Rosenbloom, N., Stone, E. J., McKay, N. P., Lunt, D. J., Brady, E. C., &
895 Overpeck, J. T. (2013). How warm was the last interglacial? new model-data
896 comparisons. *Philosophical Transactions of the Royal Society A: Mathematical,*
897 *Physical and Engineering Sciences*, 371(2001). <https://doi.org/10.1098/rsta.2013.0097>
- 898 Patterson, M. O., McKay, R., Naish, T., Escutia, C., Jimenez-Espejo, F. J., Raymo, M. E.,
899 Meyers, S. R., Tauxe, L., Brinkhuis, H., & IODP Expedition 318 Scientists (2014).
900 Orbital forcing of the East Antarctic ice sheet during the Pliocene and Early Pleistocene.
901 *Nature Geoscience*, 7(11), 841–847. <https://doi.org/10.1038/ngeo2273>
- 902 Pollard, D., & DeConto, R. M. (2009). Modelling West Antarctic ice sheet growth and
903 collapse through the past five million years. *Nature*, 458(7236), 329–332.
904 <https://doi.org/10.1038/nature07809>
- 905 Putkonen, J., Balco, G., & Morgan, D. (2008). Slow regolith degradation without creep
906 determined by cosmogenic nuclide measurements in Arena Valley, Antarctica.
907 *Quaternary Research*, 69(2), 242–249. <https://doi.org/10.1016/j.yqres.2007.12.004>
- 908 Schäfer, J. M., Baur, H., Denton, G. H., Ivy-Ochs, S., Marchant, D. R., Schlüchter, C., &
909 Wieler, R. (2000). The oldest ice on Earth in Beacon Valley, Antarctica: New evidence
910 from surface exposure dating. *Earth and Planetary Science Letters*, 179(1), 91–99.
911 [https://doi.org/10.1016/S0012-821X\(00\)00095-9](https://doi.org/10.1016/S0012-821X(00)00095-9)
- 912 Steig, E. J., Morse, D. L., Waddington, E. D., Stuiver, M., Pieter, M., Mayewski, P. A.,
913 Twickler, M.S., & Whitlow, S.I. (2000). Wisconsinan and Holocene climate history from
914 an ice core at Taylor Dome, western Ross Embayment, Antarctica. *Geografiska*
915 *Annaler: Series A, Physical Geography*, 82(2-3), pp.213-235.
916 <https://doi.org/10.1111/j.0435-3676.2000.00122.x>
- 917 Sugden, D. E., Marchant, D. R., Potter, N., Souchez, R. A., Denton, G. H., Swisher, C. C., &
918 Tison, J. L. (1995). Preservation of Miocene glacier ice in East Antarctica. *Nature*,
919 376(6539), 412–414. <https://doi.org/10.1038/376412a0>
- 920 Summerfield, M. A., Sugden, D. E., Denton, G. H., Marchant, D. R., Cockburn, H. A. P., &
921 Stuart, F. M. (1999). Cosmogenic isotope data support previous evidence of extremely
922 low rates of denudation in the Dry Valleys region, southern Victoria Land, Antarctica.
923 *Geological Society Special Publication*, 162, 255–267.
924 <https://doi.org/10.1144/GSL.SP.1999.162.01.20>
- 925 Sutter, J., Eisen, O., Wemer, M., Grosfeld, K., Kleiner, T., & Fischer, H. (2020). Limited
926 Retreat of the Wilkes Basin Ice Sheet During the Last Interglacial Geophysical
927 Research Letters. <https://doi.org/10.1029/2020GL088131>
- 928 Swanger, K. M., Babcock, E., Winsor, K., & Valletta, R. D. (2019). Rock glaciers in Pearse
929 Valley, Antarctica record outlet and alpine glacier advance from MIS 5 through the
930 Holocene. *Geomorphology*, 336, 40–51.
931 <https://doi.org/10.1016/j.geomorph.2019.03.019>
- 932 Swanger, K. M., Lamp, J. L., Winckler, G., Schaefer, J. M., & Marchant, D. R. (2017). Glacier
933 advance during Marine Isotope Stage 11 in the McMurdo Dry Valleys of Antarctica.
934 *Scientific Reports*, 7(September 2016), 1–9. <https://doi.org/10.1038/srep41433>
- 935 Swanger, K. M., Marchant, D. R., Schaefer, J. M., Winckler, G., & Head, J. W. (2011).
936 Elevated East Antarctic outlet glaciers during warmer-than-present climates in southern
937 Victoria Land. *Global and Planetary Change*, 79(1–2), 61–72.
938 <https://doi.org/10.1016/j.gloplacha.2011.07.012>



- 939 Turney, C. S. M., Fogwill, C. J., Golledge, N. R., McKay, N. P., van Sebille, E., Jones, R. T.,
940 Etheridge, D., Rubino, M., Thornton, D. P., Davies, S. M. and Ramsey, C. B., *et al.*
941 (2020). Early Last Interglacial ocean warming drove substantial ice mass loss from
942 Antarctica. *Proceedings of the National Academy of Sciences of the United States of*
943 *America*, 117(8), 3996–4006. <https://doi.org/10.1073/pnas.1902469117>
- 944 Wilcken, K. M., Fujioka, T., Fink, D., Fülöp, R. H., Codilean, A. T., Simon, K., Mifsud, C., &
945 Kotevski, S. (2019). SIRIUS Performance: ^{10}Be , ^{26}Al and ^{36}Cl measurements at
946 ANSTO. *Nuclear Instruments and Methods in Physics Research, Section B: Beam*
947 *Interactions with Materials and Atoms*, 455, 300–304.
948 <https://doi.org/10.1016/j.nimb.2019.02.009>
- 949 Wilson, D. J., Bertram, R. A., Needham, E. F., Flierdt, T. Van De, Welsh, K. J., McKay, R. M.,
950 Mazumder, A., Riesselman, C.R., Jimenez-Espejo, F.J., & Escutia, C. (2018). Ice loss
951 from the East Antarctic Ice Sheet during late Pleistocene interglacials. *Nature*,
952 561(7723), 383–386. <https://doi.org/10.1038/s41586-018-0501-8>
- 953 Yan, Y., Spaulding, N. E., Bender, M. L., Brook, E. J., Higgins, J. A., Kurbatov, A. V., &
954 Mayewski, P. A. (2021). Enhanced Moisture Delivery into Victoria Land, East
955 Antarctica During the Early Last Interglacial: implications for West Antarctic Ice Sheet
956 Stability. *Climate of the Past*, 17(5), 1841-1855. [https://doi.org/10.5194/cp-17-1841-](https://doi.org/10.5194/cp-17-1841-2021)
957 2021
- 958 Yershov, E. D. (1998). *General Geocryology. Studies in Polar Research.* (P. J. Williams,
959 Ed.). Cambridge: Cambridge University Press.
960 <https://doi.org/doi:10.1017/CBO9780511564505>
- 961
- 962
- 963